From Darcy to Turbulent Flow: Investigating Flow Characteristics and Regime Transitions in Porous Media

R. Abdi[1*], M. Krzaczek[1] and M. Abdi[2]

[1]Faculty of Civil and Environmental Engineering, Gdansk University of Technology, 80-233 Gdańsk, Narutowicza 11/12, Poland

[2]School of Engineering and Sustainable Development, De Montfort University, LE1 9BH Leicester, UK

rezvan.abdi@pg.edu.pl, marek.krzaczek@pg.edu.pl, meisam.abdi@dmu.ac.uk

Abstract

This research addresses the flow characteristics within a porous medium composed of a monolayer of closely packed spheres, spanning from viscous-dominated to turbulent flow regimes. In the first part of this paper, the turbulent flow characteristics at a 30 MPa pressure drop within the domain are presented. The results are averaged across different cross-sections between the inlet and outlet. In the second part of the study, simulations are conducted with pressure drops, ranging from nearly 0 to 100 MPa. The analysis finds distinct flow patterns within the domain and provides estimations for the permeability and the inertial term coefficient. Moreover, the transition from Darcy to non-Darcy and turbulent flow is achieved through the use of different criteria. The specified geometry is suitable for validating and calibrating simplified Discrete Element Method (DEM) models coupled with Computational Fluid Dynamics (CFD). The main goal of this research is to produce a reliable benchmark to figure out the challenge of limited experimental data concerning fluid flow characteristics in densely packed granules specially subjected to high pressure conditions. To do this, representative specimens are designed, accurate simulations are conducted, and precise assessments of the results are carried out.

Keywords: porous media; permeability; spheres; Darcy; packed bed; DEMCFD.

Latin symbols

A	cross-section area [m^2]
A_t	total cross-section area (area of fluid and solid) [m^2]
D	sphere diameter [mm]
D_e	equivalent sphere diameter [m]
$\acute{I}$	turbulence intensity
k_{TKE}	turbulent kinetic energy per unit mass [m^2s^{-2}]
$\overline{k_{TKE}}$	mean turbulent kinetic energy per unit mass [m^2s^{-2}]
K_D	Darcy permeability coefficient [m^2]
K_F	Forchheimer permeability coefficient [m^2]
K_{app}	apparent permeability coefficient [m^2]
K^*	non-denominational permeability
L	(streamwise) length of the specimen [m]
n	number of elements [million]
P	fluid pressure [Pa]
P_0	reference fluid pressure [Pa]
$\bar{P}$	average fluid pressure [Pa]
P_k	shear production of turbulence [kg/ms^3]
$P_{kb}, P_{\omega b}$	buoyancy production of turbulence in k/ω-equation [kg/ms^3]
Q	volumetric flow rate [m^3/s]
R	sphere radius [m]
Re	Reynolds number
Re_k	permeability Reynolds number
Re_{part}	particle Reynolds number
S_A	surface area of particles [m^2]
t	Time [s]
U_s	superficial velocity [m/s]
V	fluid velocity [m/s]
$\bar{V}$	average fluid velocity [m/s]
V_P	volume of granular particles [m^3]

x, y, z	*x, y, z* - coordinate [m]

Greek symbols

$\alpha, \beta', \beta_{\mathrm{i}}$	BSL model constants
β	(Forchheimer) inertial coefficient
ε	dissipation rate of turbulent kinetic energy k_{TKE} [m^2/s^{-3}]
ζ	vorticity [s^{-1}]
μ	dynamic viscosity [Pa s]
μ_t	eddy viscosity [Pa s]
ξ	viscosity ratio (μ_t/μ)
$\bar{\xi}$	mean viscosity ratio
ρ	density [kg/m^3]
$\bar{\rho}$	mean density [kg/m^3]
σ_k, σ_ω	turbulent Prandtl number
τ	tortuosity
ϕ	porosity
ω	turbulent frequency [1/s]

Abbreviations

BSL	Baseline Reynolds stress model
CFD	computational fluid dynamics
DEM	discrete element method
FVM	finite volume method
KE	(total) kinetic energy
LBM	Lattice Boltzmann method
MRI	magnetic resonance imaging
RMS	root-mean-square
RSM	response surface method
2D	two-dimensional
3D	three-dimensional

1. Introduction

Enormous applications of fluid flow through porous media can be observed in different technology fields. Examples of such flow can be found in the oil and gas production industry [1], [2], filters, heat exchangers, chromatography columns, chemical reactors [3], iron industry [4], [5] and manufacturing of composites [6], [7]. The intricate and tortuous flow paths within porous materials have an effect on the complexity of fluid flow characteristics. The interactions between solid and fluid within these complex pathways can result in a change in fluid pressure. Prior studies have identified various flow patterns, ranging from creeping to turbulent, within porous materials [8-10]. However, as a result of the flow field's complexity, many aspects remain unclear [11].

Various experimental and numerical methods have been utilized in the literature for the study of porous media. Numerical studies typically employ either the lattice-Boltzmann method (LBM) [12]-[18] or the finite volume method (FVM) [1], [2], [19], [20]. Experimental studies are commonly conducted using tomographic or optical methods, which can incur significant costs and may yield low-resolution results [21]-[23]. To simplify the complexity of the problem, numerous simplifications have been applied in both numerical and experimental studies. For instance, in the experimental work conducted by Khayamyan et al. [24], [25], porous media were created using parallel tubes, disregarding the intricacies of real geometry. In a more precise experimental work [26], flow over packed beds of spheres was modeled; however, the overlap among spheres was not considered. This exclusion may be because of the particular objectives of the experiment or because of difficulties in assembling the appropriate experimental setup. Similarly, numerical investigations frequently ignore the overlap between spheres, possibly to focus on particular features of the topic being studied or to facilitate mesh generation and speed up the simulations [10], [12], [14], [19], [20], [27].

Using three-dimensional X-ray images of a stone specimen, Muljadi et al. [28] simulated fluid flow through the real specimen. In addition, they conducted simulations to describe the flow through an artificial specimen of closely packed spheres, ignoring the consideration of any overlaps. Although there has been significant research on flow within porous media, further investigations are needed to gain an in-depth knowledge of the complex flow characteristics at the pore scale, specifically in scenarios that involve mechanical/fluid coupling, multi-scale effects, and heterogeneous materials.

Therefore, future study needs to focus on these elements to better understand fluid flow inside porous materials.

Recently, the most interesting problem has been the interaction between mechanical response of the porous material skeleton and physical phenomena such as fluid flow and heat transfer. This issue is especially critical in certain engineering applications where the complex fluid-solid interactions at the meso or micro scales become crucial. This highlights the significance of using DEM-CFD models in order to correctly describe such complex phenomena. Although DEM is becoming increasingly popular for recreating the skeleton structure of porous materials, the main difficulty lies in coupling the mechanical model with models of physical phenomena.

Meso-scale DEM-CFD models, such as those used to simulate fracture propagation in shale rocks during the hydraulic fracturing process (a technique used to increase the network of rock fractures by injecting fluid at high pressure to extract shale gas and oil), face challenges related to calibration and validation [1], [2]. Given that the porosity of natural shale rock reservoirs generally ranges from 0.5% to 10% [29] and their permeability typically falls between (10-100) $\times 10^{-15}$ m^2 [29], these simulations require a model capable of accurately capturing both solid and fluid domains at the meso level within a reasonable simulation time. Among existing models, employing a fluid flow network composed of channels in the continuous domain between particles in coupled DEM-CFD solvers is crucial. However, the fluid model in coupled DEM-CFD solvers is reduced to a system of channels, and more accurate data are needed for calibration and validation of the model. Figure 1 illustrates a fluid flow network model where the fluid moves through channels rather than within the particles. Artificial channels are depicted in green and connect particles that are in contact with each other, whereas the actual channels are shown in red and connect the centers of adjacent pores. The primary benefit of these coupled DEM-CFD models is their capacity to calculate the topology change of porous media specimens with low porosity and permeability in a reasonable amount of time.

Regardless of the simplifications used in the fluid flow model, the main difficulty in the study of porous materials at the meso-scale level is the assessment of the compliance of the fluid flow characteristics between the model and reality [1], [2]. For instance, the coupled DEM-CFD models assume laminar flow within the channels. The validity of this assumption should be examined to determine its feasibility. The fluid flow model validation can be performed experimentally or

numerically. The most reliable method of fluid flow model validation is to compare the calculation results with the results of experimental measurements. However, experiments of fluid flow in porous materials at the meso-scale are very difficult and limited. Real field data or laboratory experimental data cannot be used to validate and calibrate these simple models, where the fluid flow is limited to 2D. Therefore, an accurate numerical model is necessary to calibrate and validate the DEM-CFD models. This accurate numerical model should demonstrate its precision through validation with experimental data.

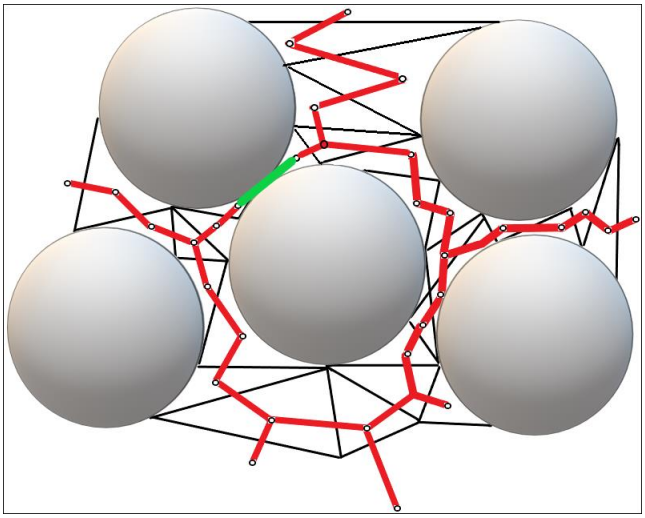

Fig.1: 2D CFD model strongly coupled with the DEM model (2D DEM-CFD). This approach is based on the concept of a fluid flow network consisting of channels connecting pores and capillaries within the continuous space of the porous material framework.

Three crucial parameters in the study of porous media are porosity ($\emptyset$), superficial velocity (U_s), and Darcy permeability (K_D). The proportion of the volume occupied by fluid (known as pore volume) to the overall volume within the porous domain (comprising both fluid and solid volumes) is called porosity. As the velocity within different sections of porous media can vary significantly, superficial velocity provides an average velocity over each section (which includes both solid and fluid areas) and remains constant across the entire porous domain in the steady fluid flow. Darcy

permeability (K_D) shows the ability of a porous material to allow fluid to flow through its pores. Sound prediction of K_D is critical in porous media studies, as it is required, for instance, to assess the natural underground flow of gases or water [18]. In this research, we need to explain permeability and Darcy's law in detail. The reason for this is explained in the following paragraph.

A common physical value that can be determined in the laboratory is permeability K_D. In addition, the K_D can be estimated using a semi-empirical equation called Darcy's law, which has several limitations. The meso scale DEM-CFD models for simulation of fluid flow in a porous material with very low porosity are typically calibrated based on bulk permeability in practice [2]. Although calibration based on permeability is widely used, it can lead to significantly inaccurate results. For example, the hydraulic fracture growth in hydraulic fracturing process can differ considerably between two specimens with the same permeability. Therefore, an accurate numerical model (not a simplified one, such as a network of channels) is essential to validate and calibrate the DEM-CFD models.

The quantification of K_D can be achieved directly and precisely using a well-known semi-empirical equation called Darcy's law. This equation was originally derived to measure pressure drop inside porous media at low Reynolds numbers, which constitute a purely viscous regime:

$$-\nabla P = \frac{\mu U_s}{K_D} \tag{1}$$

The equation represents the change in pressure (∇P) over a certain distance, and the symbol μ represents the dynamic viscosity.

Estimating permeability in the Darcy viscous regime can offer a more precise representation of the actual structure within a porous media [30]. In contrast to higher Reynolds numbers, where disturbances such as wakes, boundary layers, and inertial cores appear [31], in the Darcy viscous regime, flow streamlines closely conform to the physical structure of the porous medium.

Darcy's law does not include parameters like characteristic pore size, porosity, tortuosity, or connectivity, which are the parameters controlling K_D. There are different formulas for determining Darcy permeability, K_D, in the literature. Two well-known formulas are the Carman-Kozeny equation developed semi-empirically [32]-[34] (Eq.7) and the van der Hoef equation developed through LBM [16] (Eq.8).

The primary challenge associated with these permeability prediction equations is their limited applicability, which arises from the assumptions on which they were developed [15]. Previous studies [35]-[37] have discovered deviations from the Darcy equation at low velocities. The Darcy equation is inappropriate for calculating the properties of a region with significant boundary layers since it does not account for any microscopic shear effects [10]. As the Reynolds number increases, the flow regime transitions gradually from Darcy flow to non-Darcy flow. Multiple studies have examined the transition from Darcy to non-Darcy regimes. This is particularly important in industries such as oil and gas extraction [10], [38], [39]. An effective prediction of oil and gas flow characteristics and calculation of production performance relies significantly on an in-depth knowledge of the flow regime. The onset of inertial flow, and ultimately turbulence, occurs in some pores before others as the overall Darcy velocity or Reynolds number increases. Nevertheless, this phenomenon has received limited attention in existing published data [10]. Increasing the Reynolds number introduces inertial forces that lead to additional pressure drop (Δp) in the specimen. This results in a non-linear relationship between velocity and Δp. Numerous investigators have incorporated different terms into the Darcy equation in order to address the influence of inertial forces on Δp [10]. The proposed equation by Burke and Plummer [40], exclusively considers fully turbulent flow regimes. In contrast, Ergun suggested an equation capable of applicability across both laminar and turbulent regimes [41]. This equation can be restructured through a comparison with the Forchheimer equation. The last form it takes is Eq.2. The second term on the right side represents the pressure drop caused by inertial forces [10]:

$$-\nabla P = \frac{\mu U_s}{K_F} + \rho\beta {U_s}^2 \tag{2}$$

where K_F ($= \frac{{D_e}^2\phi^3}{150(1-\phi)^2}$ in the Ergun equation denoted as the Forchheimer permeability coefficient, and it is similar but not identical to K_D [28]. Additionally, β ($= \frac{1.75(1-\phi)}{\phi^3 D_e}$ in the Ergun equation) defined as the inertial coefficient. Here, ρ represents density, and D_e is the equivalent particle diameter. Several coefficients have been suggested in the literature for computing K_F and β in Eq.2. For example, instead of utilizing the numbers of 150 for the calculation of K_F and 1.75 for β in the Ergun equation, some scientists have proposed other values such as 200 for K_F and 1.75 for β [42], or 180 for K_F and a range of 1.8 to 4.0 for β [43]. It should be emphasized that these coefficients may differ based on the flow conditions and geometry [19], [44]. Some equations

available for determining ∇P, K_D, and β are more suitable for particular geometry and conditions from which they are derived. Using them for alternative geometries may yield inaccurate outcomes. Therefore, in this research, the values of K (using Eq.1) and β (using Eq.2) are directly obtained and compared with values obtained from well-known equations, such as the Ergun, Carman-Kozeny, and van der Hoef equations.

The velocity distribution and streamlines should be analyzed in detail to have a precise understanding of transport within the porous domain [45]. Hence, another important goal of this study is to investigate flow characteristics at the pore level within the inter-grain regions over a wide range of velocities, spanning from creeping to turbulent flow. To unveil the intricacies of flow structure, the velocity streamlines are studied and discussed precisely as Re increases. The driving force for fluid flow in the present study is the pressure differential (Δp) across the top and bottom boundaries of the porous specimen, varying from nearly 0 to 100 MPa. The fluid is assumed to be incompressible and single phase. A thorough examination of the flow field at 30 MPa, a pressure relevant to the hydraulic fracturing process is initially presented. Turbulent variables and velocity streamlines are illustrated and discussed with the Baseline (BSL) Reynolds Stress model, employed for solving the Reynolds-averaged Navier-Stokes equations in the turbulent regime.

In this study, a porous medium is modeled using 131 monodisperse spheres, each with a diameter of 1 mm. The spheres are arranged in a single layer with significant overlap. While these overlaps are intentionally introduced to control porosity, this approach differs from real systems where porosity variations typically result from grain-size distribution or non-spherical particle shapes. Therefore, it is important to mentioned that this method of adjusting porosity may not fully capture the complexities of natural porous media. This particular geometry, with specific boundary conditions, is studied due to its relevance to our research and other studies related to coupled DEM-CFD. The choice of spherical discrete elements was intended to slightly simplify the geometry of the physical system. The geometry, with a porosity of 34%, can serve as a reliable benchmark for calibrating and validating 2D/3D DEM-CFD models, such as those presented in [46]-[49]. As discussed, the DEM-CFD models are often simplified (e.g., [1], [2], [46]-[49]) where the fluid domain is restricted to 2D. Consequently, real 3D experimental or numerical data cannot be utilized for model calibration. Similar geometries were utilized in our previous studies [1], [2] to calibrate and validate the DEM-CFD model. Therefore, the goal of this work is not to calibrate the DEM-

CFD model. For details on the calibration and validation process, please refer to our earlier publications [1], [2]. The presented novel benchmarking method can be used directly to calibrate and validate any existing 2D DEM-CFD model intended to study physical phenomena at meso- and micro-level. Therefore, for developing accurate numerical CFD model, commercial CFD software was chosen.

ANSYS CFX V19 which uses the finite volume method (FVM) is used for flow simulation within the voids between the spheres. The validity of the FVM model is assessed by comparing the results with corresponding experimental data [26] and numerical data [14], [20] from the literature. This study offers a comprehensive and reliable resource for future investigations concerning porous media. Precise values for permeability and inertial coefficients are obtained from simulation results and compared with widely used correlations such as the Kozeny-Carman, Ergun, and van der Hoef models. Additionally, we estimate and discuss tortuosity. This study differentiates itself from previous works through:

- Utilizing a distinct geometry that is better suited for calibrating and validating DEM-CFD codes.
- Considering a wide range of Reynolds number, from very low to high, with detailed visualizations of flow characteristics.
- Capturing the onset and the corresponding Reynolds numbers of the non-Darcy regime, the change in flow regime from laminar to turbulent, as well as the fully inertial regime. Furthermore, proposing a non-dimensional permeability for both transient and fully turbulent regimes.

In the present study, the methodology and governing equations are explained in Section 2. The validation is presented in Section 3. The specimen, boundary conditions, and meshing process are detailed in Section 4. The results for $\Delta p = 30$ MPa are presented in Section 5. In Section 6, a more elaborate study for various Δp values is conducted, and the permeability and inertial coefficient are calculated. Finally, the summary, conclusion, and future work are presented in Section 7.

2. Methodology and governing equations

The governing equations representing both laminar and turbulent flow regimes inside a porous medium are the continuity (Eq. 3) and Navier-Stokes (Eq. 4) equations, which originate from the conservation of mass and momentum laws, respectively.

$$\frac{\partial \rho}{\partial t} + \nabla.(\rho V) = 0, \tag{3}$$

$$\frac{\partial (\rho V)}{\partial t} + \nabla.(\rho VV) = -\nabla P + \mu \nabla^2 V \tag{4}$$

where t is time, P denotes the fluid pressure, and V is the fluid velocity. Gravitational forces are neglected in these equations.

In the literature, various definitions for Reynolds number exist [50]. In this study, the particle Reynolds number (Eq. 5) and the permeability Reynolds number (Eq. 6) are used to investigate the flow characteristics in a porous medium. The particle Reynolds number (Re_{part}) is applicable when the porous medium is composed of spheres, and permeability (Re_K) number is useful for distinguishing between Darcy and non-Darcy flow regimes [28].

$$Re_{part} = \frac{\rho\, Us\, D_e}{\phi\, \mu} = \frac{\rho\, \overline{Vy}\, D_e}{\mu}, \tag{5}$$

$$Re_K = \frac{\rho\, Us\, \sqrt{K_D}}{\mu}, \tag{6}$$

where $\overline{Vy}$ is the average streamwise velocity in the pores, ϕ denotes the porosity and K_D is the Darcy's permeability. The equivalent diameter of particles, $D_e = \frac{6V_P}{S_A}$, where V_P is the volume of the granular particles and S_A is the surface area of those particles, is used for the calculation of Re_{part}. The superficial velocity is defined as $U_s = Q / A_t$, where A_t is the total cross-sectional area of the specimen perpendicular to the main flow direction, and Q is the volumetric flow rate. By increasing the particle Re number above 120, highly chaotic structures have been observed in the literature [35]. As discussed earlier, the precise value of Darcy's permeability coefficient K_D can

be found from the Darcy law (Eq.1), which requires understanding of flow features, including pressure and velocity. Alternatively, K_D in Eq.6 can be estimated by utilizing the Carman-Kozeny (Eq.7) or van der Hoef (Eq.8) equations, which are only based on geometrical properties of the specimen:

$$K_D = \frac{{D_e}^2}{180}\frac{\phi^3}{(1-\phi)^2} \tag{7}$$

$$K_D = {D_P}^2\left(180\frac{(1-\phi)^2}{\phi^3} + 18\phi(1-\phi)\left(1+1.5\sqrt{1-\phi}\right)\right)^{-1} \tag{8}$$

This research utilized a laminar model to analyze situations with small values of pressure drop, Δp, which resulted in low Reynolds numbers (Re). As the Reynolds number (Re) grows, crossing the threshold where the influence of inertial forces becomes much more than that of viscous forces, the flow tends towards turbulence. This leads to the oscillating motion of components of fluid inside the domain. As a result, velocity and other flow variables can be divided into fluctuating and average terms. For example, the velocity v can be separated into a fluctuated component v' and an averaged component $\bar{v}$. The fluctuating terms cover the turbulence effect. By employing an averaging procedure on the governing equations (Eqs. 3 & 4), these terms are eliminated or 'smoothed,' resulting in simplification of the equations. Nevertheless, the averaging process introduces additional stresses (Reynolds stresses) in Eq.4, which remain unknown and necessitate additional equations from various turbulent models to close the equation set [19]. At higher Re values, the turbulent model was implemented during simulations. The Baseline (BSL) scheme was applied to study the turbulent flow and to calculate the Reynolds stresses. The precision of this model lies in its use of six additional equations to comprehensively account for all Reynolds stresses, allowing it to accurately simulate the flow fields. The model addresses equations for the turbulent frequency (ω) as well as turbulent kinetic energy (k_{TKE}) [51]. The turbulent kinetic energy is defined by:

$$\mathrm{k}_{TKE} = 0.5(\overline{u'u'} + \overline{v'v'} + \overline{w'w'}) \tag{9}$$

where $u', v',$ and w' represent the velocity oscillations in the *OX*, *OY,* and *OZ* directions, respectively. The BSL approach converts the $\mathrm{k}_{TKE} - \omega$ model (preferred for turbulence zones with

a small Reynolds number) close the surface to the $k_{TKE} - \varepsilon$ model further from the surface inside the fluid domain. The BSL approach is presented through the k_{TKE}-equation (Eq.10) and the ω-equation (Eq.11) as follows:

$$\frac{\partial}{\partial t}(\rho k_{TKE}) + \frac{\partial}{\partial x_j}\left(\rho \bar{v}_j k_{TKE}\right) = P_k + P_{kb} - \beta' \rho k_{TKE}\omega + \frac{\partial}{\partial x_j}\left[\left(\mu + \frac{\mu_t}{\sigma_{k3}}\right)\frac{\partial(k_{TKE})}{\partial x_j}\right] \quad (10)$$

$$\frac{\partial}{\partial t}(\rho\omega) + \frac{\partial}{\partial x_j}\left(\rho \bar{v}_j \omega\right) = \alpha_3 \frac{\omega}{k_{TKE}} P_k + P_{\omega b} - \beta_{i3}\rho\omega^2 + \frac{\partial}{\partial x_j}\left[\left(\mu + \frac{\mu_t}{\sigma_{\omega 3}}\right)\frac{\partial(\omega)}{\partial x_j}\right] + \\ +(1 - F_1)2\rho\frac{1}{\sigma_{\omega 2}\omega}\frac{\partial(k_{TKE})}{\partial x_j}\frac{\partial(\omega)}{\partial x_j}, \quad (11)$$

where F_1 is the blending function, which has a fixed value of one on the surface and reduces to 0 outside of the boundary layer. The variable $\mu_t \left(= \frac{\rho k_{TKE}}{\omega}\right)$ denotes the turbulent viscosity or eddy viscosity, P_k denotes the generation of turbulence due to viscous forces, and P_{kb} and $P_{\omega b}$ represent the buoyancy generation of turbulence that signify the impact of buoyancy forces. The variable ω denotes the turbulence frequency, and $\beta'(= 0.09)$ is a constant in the BSL model. The quantities α, β_i, and the turbulent Prandtl numbers (σ_k and σ_ω) are selected from a set of constants corresponding to the ω - based model and the ε- based model [51]. If the solver is required to compute ω-region values, it considers $\alpha_1 = 0.553$, $\beta_{i_1} = 0.075$, $\sigma_{\omega 1} = 2, \sigma_{k1} = 2$. For ε-region values, the solver uses $\alpha_2 = 0.44, \beta_{i_2} = 0.0828, \sigma_{\omega 2} = 1/0.856$, and $\sigma_{k2} = 1$ [51].

3. Validation

To validate our 3D-FVM solver, we used the experimental results from Suekane et al. [26], which investigated fluid flow through cubic packed spheres (with spheres arranged at each corner of the cube as shown in Fig. 2). The volumetric porosity ϕ of the cube was 0.476. The dimensions of the cube were $28 \times 28 \times 28$ mm^3, and it contained eight fixed 1/8 spheres with a diameter of D=28 mm. Suekane et al. [26] measured fluid velocity at the cube's center using magnetic resonance imaging (MRI) technique. Water, supplied from a reservoir with a constant pressure to maintain a steady flow rate, circulated through the cube. Suekane et al. [26] observed streamwise velocities for particle Reynolds numbers Re_{part} of 12.17, 28.88, 59.78, 105.5, and 204.74. The flow regime

for Re_{part} =204.74 was reported to be laminar (as noted by Gunjal et al. [20], Chhabra et al. [52], and Seguin et al. [53], [54]). The experiment [26] was numerically modeled by Gunjal et al. [20] using the FVM commercial software ANSYS-FLUENT. In addition, Rong et al. [14] performed a similar numerical simulation employing the Lattice-Boltzmann method (LBM).

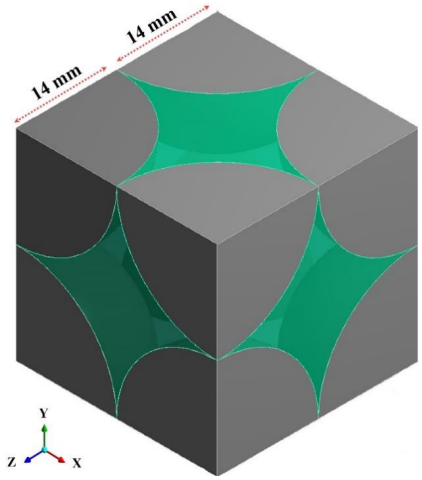

Fig.2: The specimen used for validation consists of the fluid domain (depicted in green) plus eight 1/8 spheres at each corner of the cube (depicted in gray). The origin of the coordinate system is located at the center of the cube.

The simulation was performed on an equivalent model as described in [20] using ANSYS-CFX. Water flows into the domain from the bottom boundary. At the sidewalls of the model, a symmetric condition was adopted, where only the velocity component aligned to the surface was measured. Periodicity in mass flux was applied to the top and bottom boundaries. A no-slip boundary condition was assumed on the surface of the spheres. Tetrahedral elements were used to mesh the fluid domain.

Figure 3 presents the dimensionless y-component of fluid velocities for the five different Re numbers at y=0 along the dimensionless x-value. In this figure, dimensionless velocity was used by dividing V_y by the average streamwise velocity in the fluid domain, $\bar{V}_y$. Similarly, a dimensionless distance was defined by dividing the distance x by the sphere's radius (R). As can

be seen, V_y reaches its highest amount at the center of the cube and these peaks become sharper by increasing the Re number. Hence, our FVM predictions are in great agreement with corresponding experimental [26] and numerical [14], [20] outcomes. This solver is applied to a more complicated porous domain in the following section.

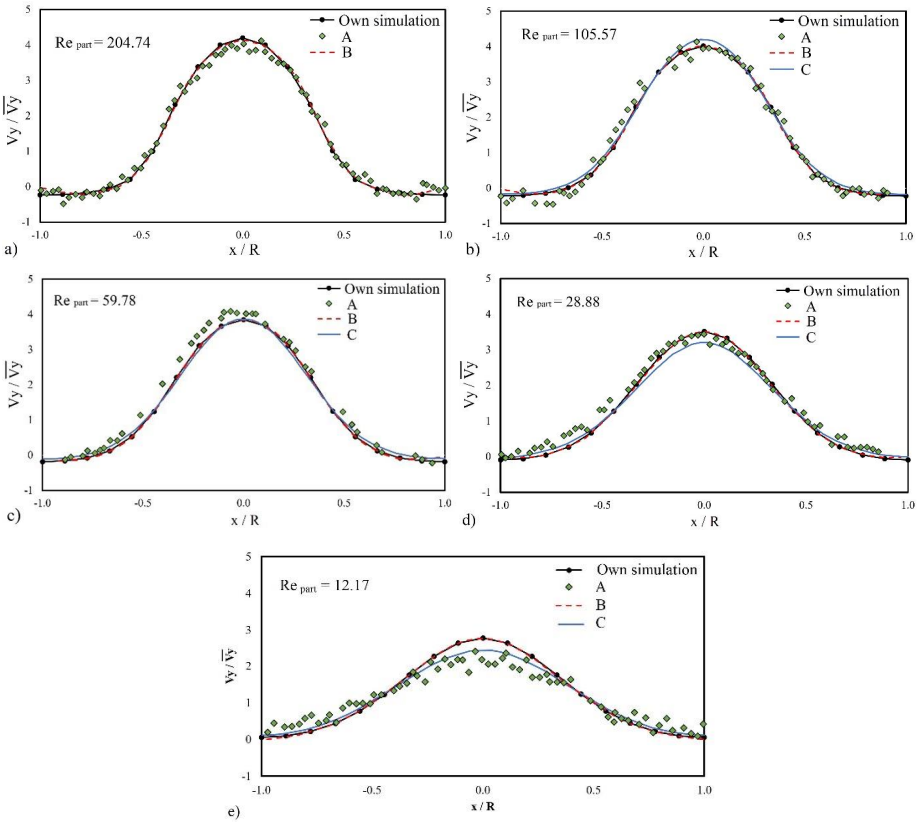

Fig.3: Dimensionless streamwise flow velocities $V_y/\overline{Vy}$ in 3D-FVM simulations at origin of unit cell (y=0) along dimensionless x-value at five different Reynolds numbers (a) Re_{part}=204.74 (b) Re_{part} =105.57 (c) Re_{part} =59.78 (d) Re_{part}=28.88 (e) Re_{part}=12.17; experimental data captured from [26] (A) FVM results [20] (B) and LBM results [14] (C).

In our previous work, another validation scenario was conducted [1]. The calculated permeabilities, K_D, were successfully compared with corresponding numerical and semi-empirical models for permeability estimation. This test involved varying the diameter of the beds at each corner of the unit cell, ranging from 0.006 m to 0.038 m, to generate different porosities. For each porosity, the K_D was determined using Eq. 1. These results were subsequently compared to the Carman-Kozeny equation (Eq. 7) and the van der Hoef equation for spherical particles (Eq. 8). The comparison revealed a good agreement between the results and the models.

4. Specimen description

The porous domain is depicted in Fig.4a. The matrix is constructed from 131 spheres that are fixed in place. The specimen initially created using DEM, and the specimen preparation technique are detailed in [55]-[57]. The geometry was then modified in AutoCAD and imported into Design Modeler software. The spheres are arranged in a single layer within a rectangular enclosure measuring 1×1×0.1 cm^3. The diameter of each sphere is 0.1 cm, with significant overlaps of maximum 0.03 cm. Hence, the final shape of the spheres was not perfectly spherical. The porous domain has a porosity of 34%.

The spheres were arranged in approximately 12 rows, and 14 indicator cross-sections were designated for describing the flow characteristics (Fig.4b). Cross-section 1 was located at the bottom of the center plane, cross-section 14 was situated over the upper side (outlet) and the other 12 cross-sections were plotted to intersect the maximum number of spheres' center in that raw. Consequently, the distances between two adjacent indicator cross-sections are not necessarily equal.

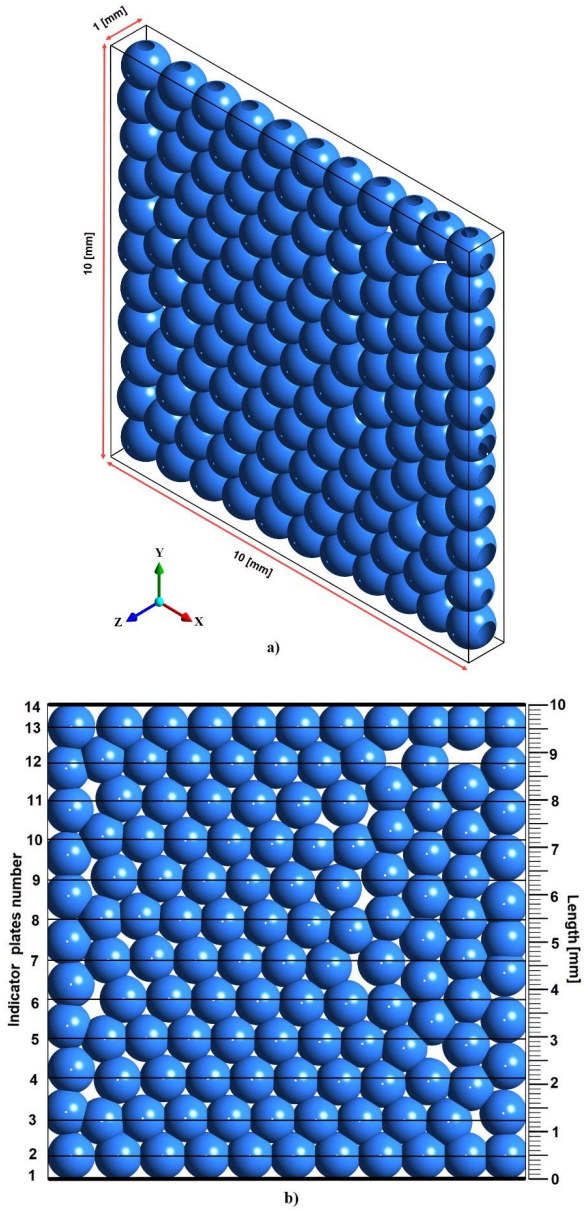

Fig.4: (a) 131 spheres specimen (b) indicator cross-sections inserted on the XY view of the specimen.

Figure 5 displays the boundary conditions of the porous specimen. The given pressure difference between the bottom and top of the specimen varies in the range of almost 0 to 100 MPa, enforcing the fluid to move from the lower wall to the upper wall of the porous medium. Shear stresses at the lateral walls are neglected, and free slip boundary conditions are applied. Shear stresses at the sphere surfaces are considered with a no-slip condition. The material properties of the working fluid are detailed in Tab.1. In simulations related to turbulent flow, a turbulence intensity I (a factor indicating velocity fluctuations) of 5% was used at both the inlet and outlet.

All simulations were conducted in steady-state mode with 400 iterations. This number of iterations was carefully chosen to ensure effective error damping, and consequently, all simulations met the convergence criteria. In this context, the highest root mean square (RMS) residual for velocity and pressure was less than 1×10^{-4}, and the RMS residual for mass flow rate was below 1×10^{-6} in all turbulent and laminar simulations.

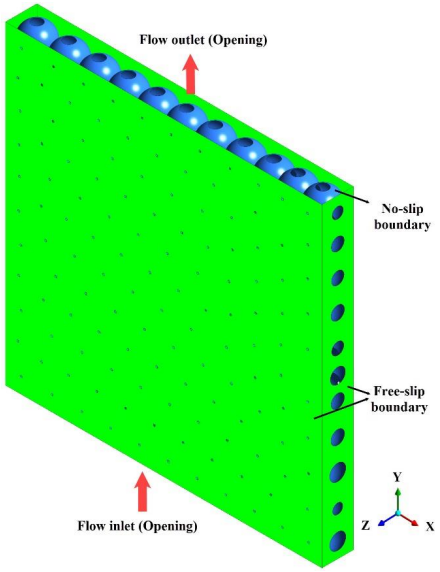

Fig.5: Boundary conditions used in the granular model illustrated in Fig.4.

Tab.1. Material properties of the working fluid, and reference values.

Material properties	Dynamic viscosity μ [Pa.s]	Reference pressure [atm]	Density [kg/m^3]
value	0.0010016	1	997

At low Re numbers (Re_{part} < 1648 or Re_k <15), a laminar model was applied, allowing for the direct solution of the Navier–Stokes equations. To consider the effect of eddies and other turbulent quantities (if present), a turbulent model was used for higher Re numbers, specifically Re_{part} > 1648 or Re_k >15, as observed at Δp = 0.039 MPa (refer to Fig.18). In case of $\xi(=\mu_t/\mu) < 5$, ANSYS User's Manual [58] suggests checking the possibility of a laminar model and comparing the results with those of the turbulent model to identify the correct regime [59]. In this study, $\xi \cong 5$ was observed at $Re_{part} \cong 6400$, showing the limit for the use of a laminar model based on the ANSYS User's Manual [58]. In this study, both models were applied within a pressure range of 3 Pa to 0.6 MPa, and good agreement between the average streamwise velocity $\overline{V_y}$ of the turbulent and laminar model was obtained up to $\Delta p = 0.039$ MPa ($\xi = 0.25$), as can be seen in Fig.6. Because of the disparity observed in results between laminar and turbulent models corresponding to $\xi > 0.25$, the starting point for adopting a turbulent model in our study was considered as $\xi \cong 0.25$, significantly below the recommended value by [58]. Additionally, Fig.6 illustrates that the BSL turbulent model accurately evaluates flow fields even in the laminar regime ($\xi < 0.25$).

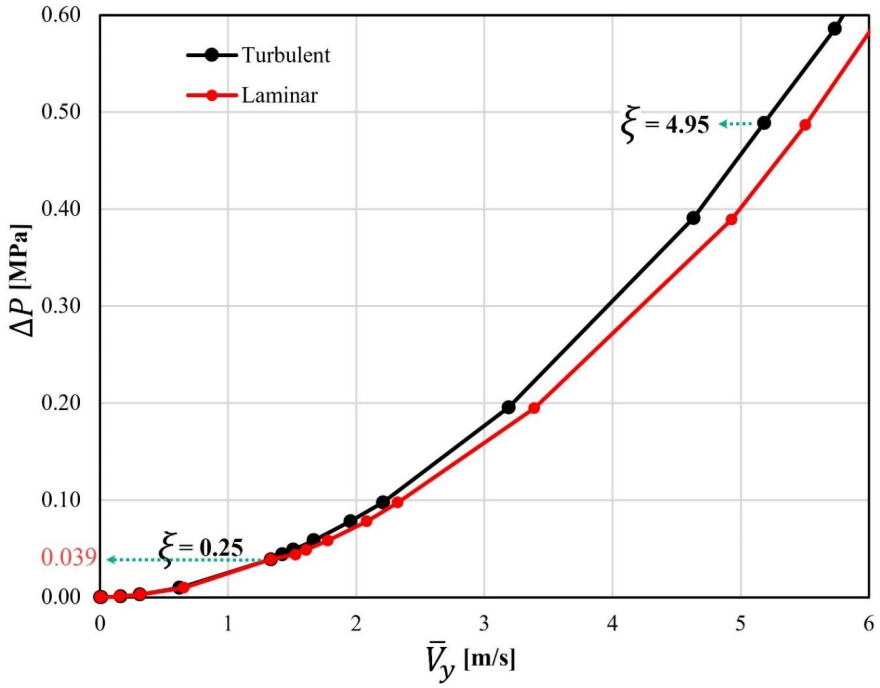

Fig.6: comparison of the mean streamwise velocity $\overline{V_y}$ between the turbulent model and the laminar model at various Δp.

Due to the overlaps between the spheres and their asymmetric arrangement, the model presents significant geometrical complexities, including numerous holes and small regions among the spheres. This makes the use of a structured mesh, as in [60], nearly impossible. Similarly, employing a thin layer of structured mesh over the spheres, where high velocity gradients occur (as in [61], [62], [63]), is not feasible in this case.

Therefore, a dense, unstructured linear tetrahedral mesh was utilized, with a significant reduction in mesh size near all sphere surfaces. The resulting model featured a mesh with a smallest element size of $2.2e^{-5}$ m, a growth rate of 1.2, and a maximum element size of $4.4e^{-5}$ m. A close-up view of the grid is shown in Fig.7. The small white circles visible in the model presented in Fig.7 are associated with missing parts of the spheres due to the contact between the sphere surfaces and the slip boundaries at the sides of the specimen, as illustrated more clearly in Fig. 5.

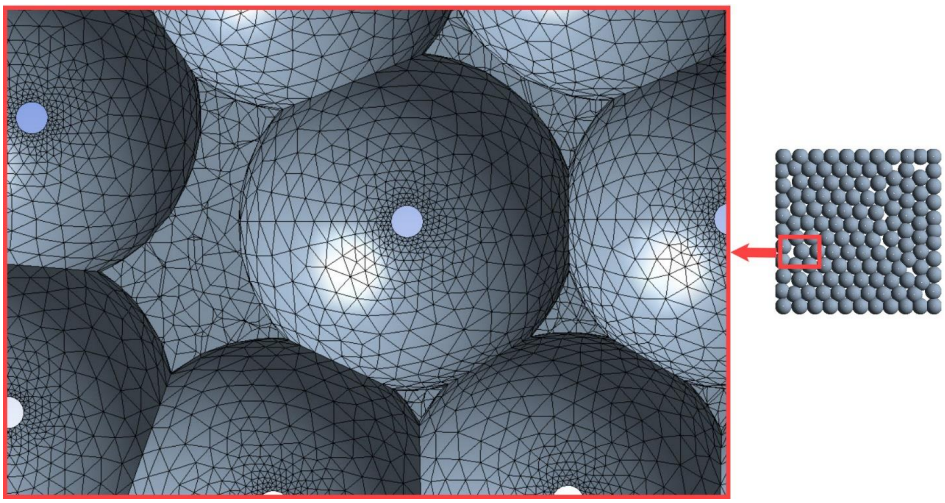

Fig.7: close-up view of the elements

The specimen with Δp = 30 MPa was chosen for the mesh dependency test. The average turbulent kinetic energy $\overline{k_{TKE}}$ and average viscosity ratio ($\overline{\xi}$, calculated as μ_t/μ) over the fluid domain were obtained for different numbers of elements. As can be seen in Fig.8, increasing the number of elements beyond 17 million did not have a significant effect on the results. In all subsequent cases, this mesh number was used for performing the simulations.

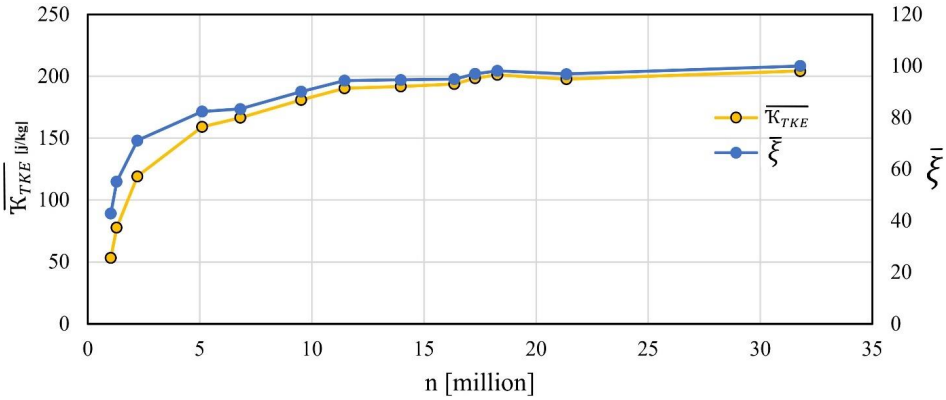

Fig.8: Mean turbulent kinetic energy $\overline{k_{TKE}}$ and mean viscosity ratio $\overline{\xi}$ in the fluid domain versus the number of elements (n).

5. Results for 30 MPa pressure drop

As an example, this section presents the results of a pressure difference (ΔP) set at 30 MPa (or 3000 $\frac{\text{MPa}}{\text{m}}$) between the inlet and outlet boundaries. A ΔP in the range of 30-40 MPa is typical for the hydraulic fracturing process. The visual representations include streamlines and contours depicting velocity (both streamwise and magnitude), vorticity, pressure (P), dynamic viscosity (μ_t), dissipation rate (ε) and turbulent kinetic energy (k_{TKE}). Each of these concepts is covered in detail.

To illustrate the changes in flow variables inside the domain, area-averaged quantities are calculated on regularly spaced horizontal cutting planes—aligned parallel to the indicator cross-sections of Fig.4b—through the domain. The mass flow rate within the porous domain has been computed to be 0.1445 kg/s, resulting to a superficial velocity (U_s) of 14.52 m/s.

Figure 9a depicts the distribution of streamwise velocity (V_y) inside the fluid domain. Within some regions, the fluid demonstrates motion in the negative Y direction, resulting in negative velocities in the plot. Notably, the fluid exhibits higher velocity at the left and right edges of each sphere in relation to the coordinate system illustrated in Fig.4. Additional information on the flow field may be found in Fig.9b, which shows the distribution of velocity magnitude (V). Since the general flow is parallel to the Y-axis, the plots of V and V_y displays a comparable distribution pattern. The flow streamlines, as presented in Fig.9c, reveal the intricate 3D flow fields. It represents the tortuous passages and swirling fluid zones. Finally, Fig.9d displays k_{TKE}, a parameter that will be further discussed in this section.

AIP Publishing Physics of Fluids ACCEPTED MANUSCRIPT

PLEASE CITE THIS ARTICLE AS DOI: 10.1063/5.0232176

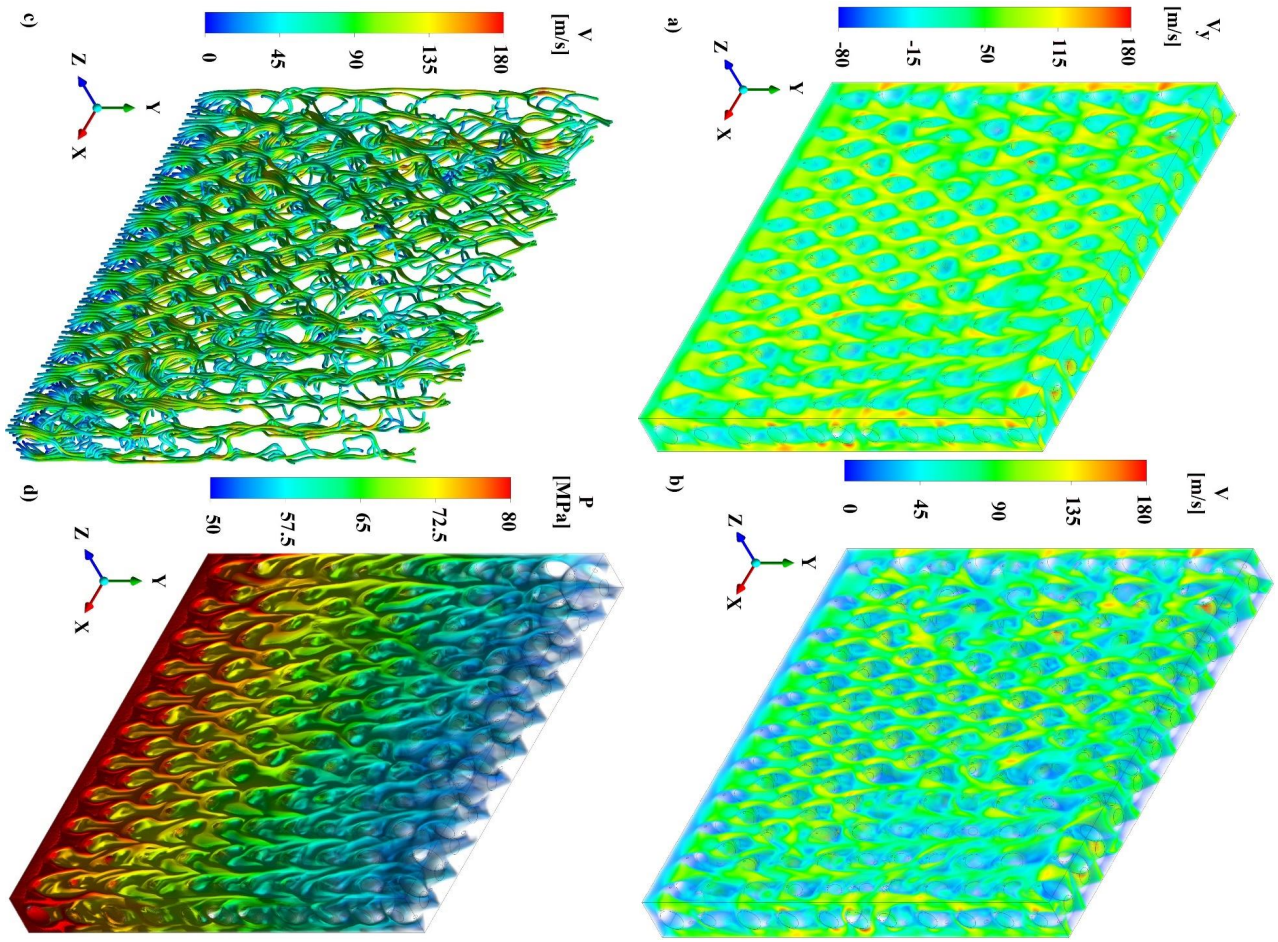

Fig.9: Flow characteristics at Δp = 30 MPa (a) streamwise velocity distribution in m/s (b) velocity magnitude distribution in m/s (c) velocity streamlines in m/s (d) total pressure distribution in MPa in the 3D domain.

The 3D streamwise velocity distribution as well as velocity magnitude were averaged over the XZ planes, and the results are presented in Fig.10a. Also, the y-coordinate values of the 14 indicator cross-sections from Fig.4b, were added to the graph in Fig.10. Both plots exhibit a similar trend with irregular variations, indicating that the primary component of velocity in the model is the streamwise component. As Fig.10b shows, fluctuations in velocity can be attributed to changes in the area in the streamwise direction (XZ plane). Constant mass flow rate in every plane (0.1445 kg/s) causes the inverse relationship between average velocity and streamwise area. Notably, on the two sides of the plot presented in Fig.10a with the largest flow area (see Fig.10b), the corresponding velocities have the lowest values. Progressing from the two sides towards the centre, the velocity reaches a maximum value of almost 90 m/s, associated with the first and last rows of spheres (cross-section numbers 2 and 13), where the flow area is the smallest. In addition, the maximum relative velocity is observed in (or close to) all other 10 indicator cross-sections because of narrow passages in the main flow direction at these locations. The small difference between the location of the maximum relative velocity and the location of indicator cross-sections (e.g., the velocity pick corresponding to indicator cross-section 12) originates from the asymmetric arrangements of the spheres.

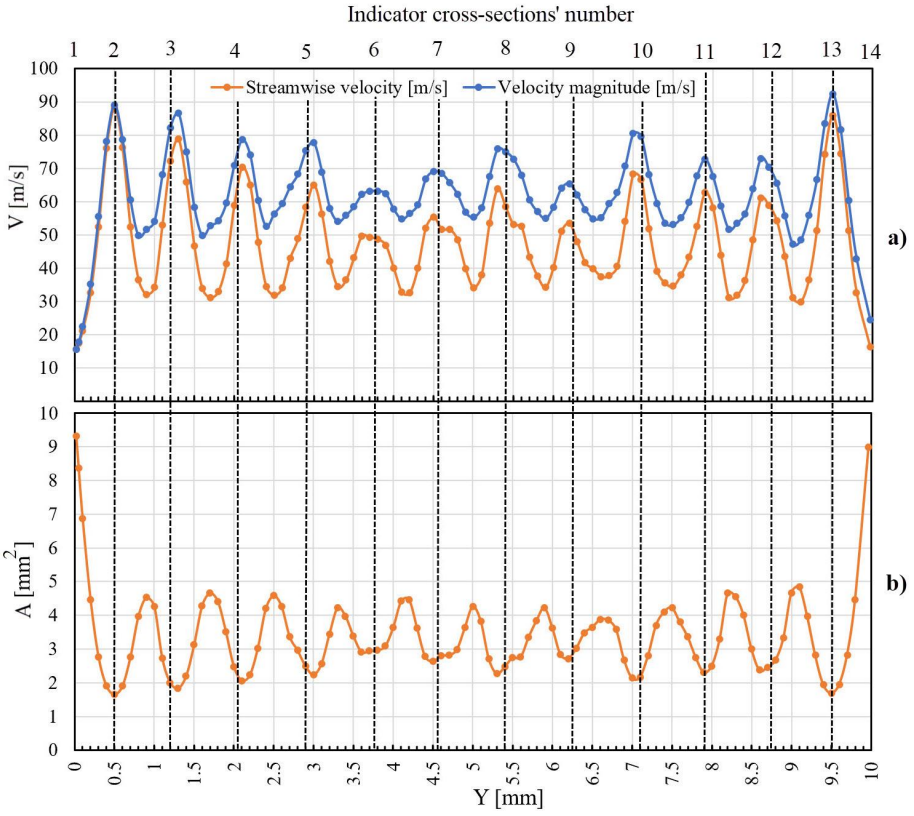

Fig.10: (a) Average streamwise velocity (V_y) and velocity magnitude (V) over the XZ planes; (b) fluid flow area (A) in the streamwise direction (XZ planes) at various Y distances through the packed specimen.

The fluid pressure distribution was averaged over the XZ planes, and the obtained findings are displayed in Fig.11. The chart clearly shows a gradual reduction in the average total pressure from 80 MPa at the inlet to 50 MPa the outlet. The mean pressure throughout the pores and voids ($\bar{P}$) was 65.7 MPa.

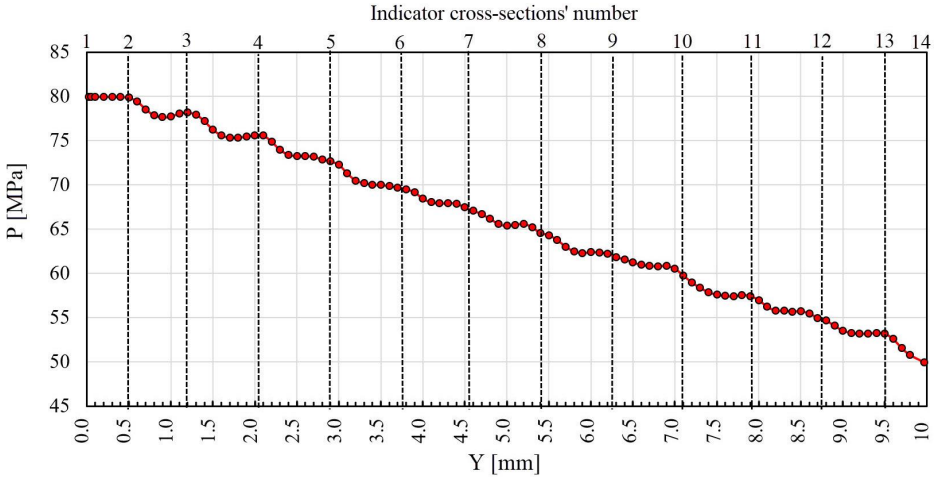

Fig.11: Average total pressure (P) over XZ planes, along with the Y distance (mm) through the packed specimen.

Geometry plays a crucial role in the turbulence generation, and the complexity of the fluid domain significantly influences turbulence generation [19]. Part of the averaged mechanical energy of the flow is converted into turbulence kinetic energy (k_{TKE}), which is then converted into heat and dissipated. Turbulence Kinetic Energy (k_{TKE}) refers to the average kinetic energy per unit mass associated with the eddies in turbulent flow. It is computed based on Eq.9, derived from the normal Reynolds stresses. The k_{TKE} is closely related to the properties of the porous material, and an increase in flow resistance results in its enhancement [64]. The 3D distribution of k_{TKE} is plotted in Fig.12a. The primary generation of k_{TKE} occurs on shear layers, with areas of elevated k_{TKE} located between the rear and side regions of each sphere with respect to the coordinate system presented in Fig.4. In the streamwise direction, k_{TKE} is successively produced at the shear layer of spheres and partially dissipates. The remaining k_{TKE} transfers to the outlet boundary. On the front side of each sphere, the amount of k_{TKE} is relatively small, gradually increasing towards the opposite side of the spheres next to the lateral walls of the specimen. The rise in value is attributed to the generation of vorticity (ζ) downstream of each sphere, as illustrated in the vorticity diagram, Fig.12b. Each sphere in the domain creates a small wake in the flow field, resulting in k_{TKE}

generation within each pore. Figure 12b illustrates clockwise/counterclockwise rotation of fluid particles on the left and right sides of each sphere, respectively. The distribution of vorticity around each sphere is not uniform due to the complex interaction of shear layers between spheres. Figures 12c and 12d show eddy dissipation ε and turbulence viscosity μ_t, which will be further discussed in detail in this section.

Figure 13a shows the average values of Reynolds stresses and k_{TKE} over the XZ planes. The magnitude of k_{TKE} is nearly zero between the inlet and the second indicator cross-section. This indicates the presence of laminar flow in this particular region. Subsequently, k_{TKE} rises gradually until it reaches 350 J/kg at the fourth indicator cross-section. It then fluctuates around 250 J/kg, with a notable decrease near the outlet. In low-velocity areas near the inlet and outlet, k_{TKE} is also small. The average Reynolds stress plots in Fig.13a fluctuate within a similar range and exhibit a comparable trend. The streamwise variations occur at slightly higher stress values compared to the other two Reynolds stresses in the figure. It shows by the blue line in Fig.13a and has a greater share in the generation of k_{TKE}.

To provide a more detailed analysis of the flow field, Fig.13b displays the average value of macroscopic kinetic energy (KE) along with k_{TKE} for comparison. The averaged k_{TKE} denoted as $\overline{k_{TKE}}$, is calculated as 216.1 J/kg. This value is roughly 11% of the mean flow kinetic energy $\overline{KE}$ (obtained as 1983 J/kg).

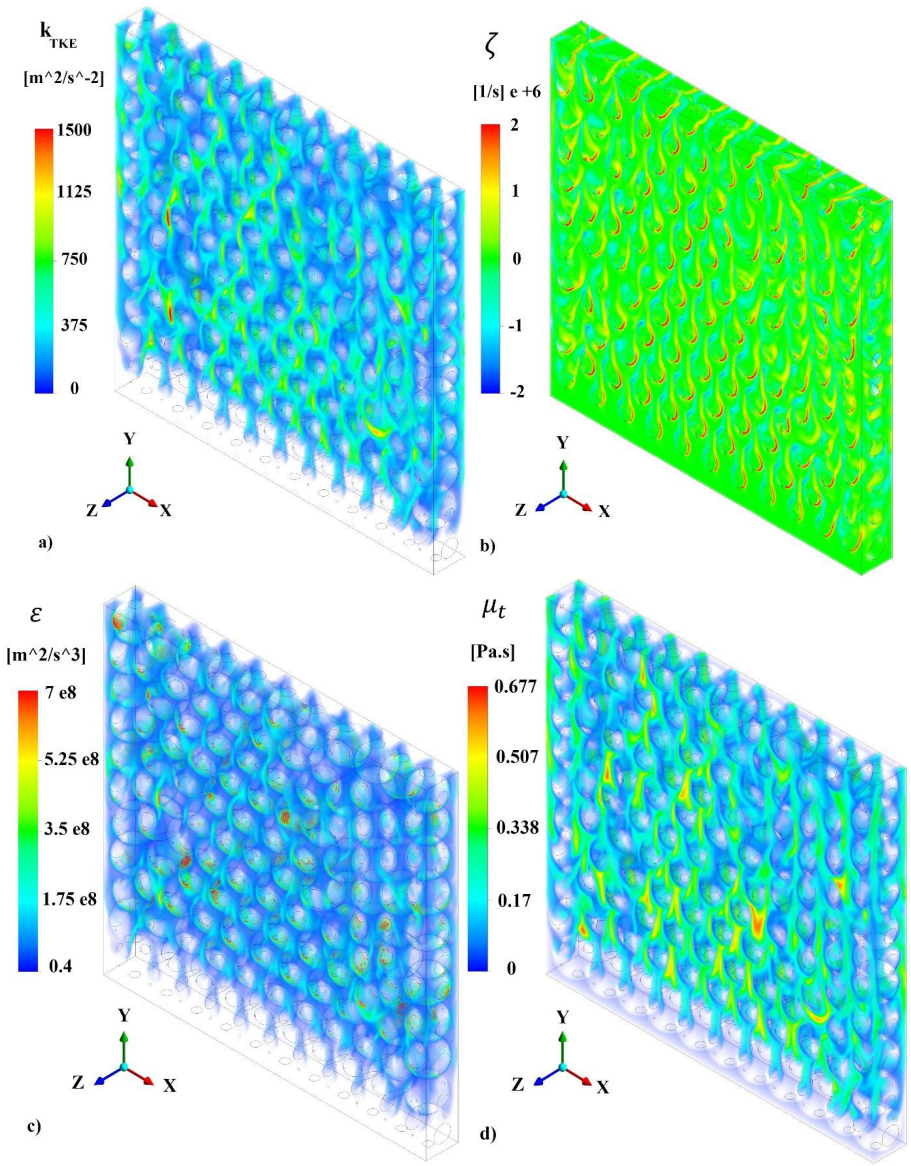

Fig.12: Turbulent variables at 30MPa (a) distribution of k_{TKE} [m^2s^{-2}] (b) out-of-plane vorticity component ζ [s^{-1}] (c) distribution of dissipation rate ε [m^2s^{-3}] (d) eddy viscosity μ_t [Pa.s] over the 3D domain.

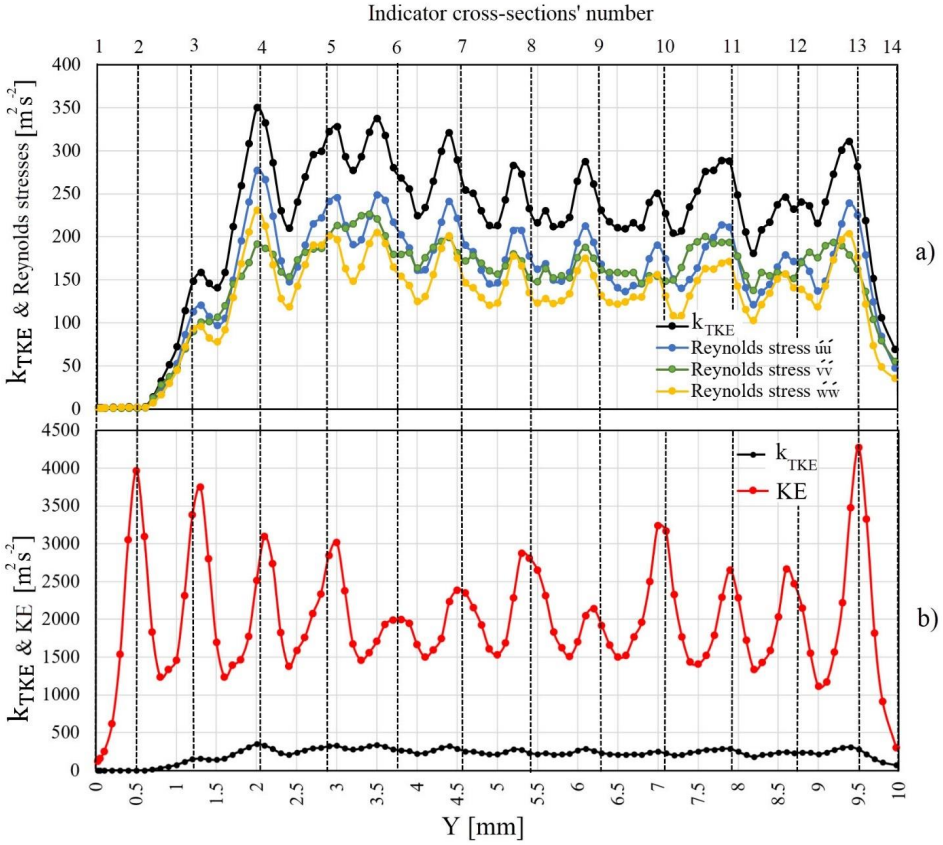

Fig.13: (a) Average k_{TKE} and Reynolds stresses over the XZ planes plotted against the Y distance through the packed specimen (b) Average mean flow KE and k_{TKE} (for comparison) over the XZ planes plotted against Y.

Figure 12c presents the turbulent eddy dissipation rate (ε), specifying the amount of energy lost due to viscous forces in the turbulent flow for the studied granular specimen. In addition, the average value of ε over different cross-sections perpendicular to main flow direction (Y axis) is presented in Fig.14. The data clearly shows a comparable pattern to the k_{TKE} plot in Fig.13a, indicating higher energy loss in regions with a greater magnitude of k_{TKE}. The highest magnitude

of ε is captured in the shear layers. It can be explained by observing the distribution of μ_t in Fig.14. The displacement of eddies from one point to another results in the transfer of energy through the turbulent flow. Eddy viscosity represents the energy transfer by relating mean shear stresses to the perpendicular component of the velocity gradient in turbulent flow. The enhanced dissipation levels detected in the shear layers of the spheres placed between the rear and sides of each sphere (Fig.12c) are caused by the high values of μ_t, as shown in the contour provided in Fig.12d.

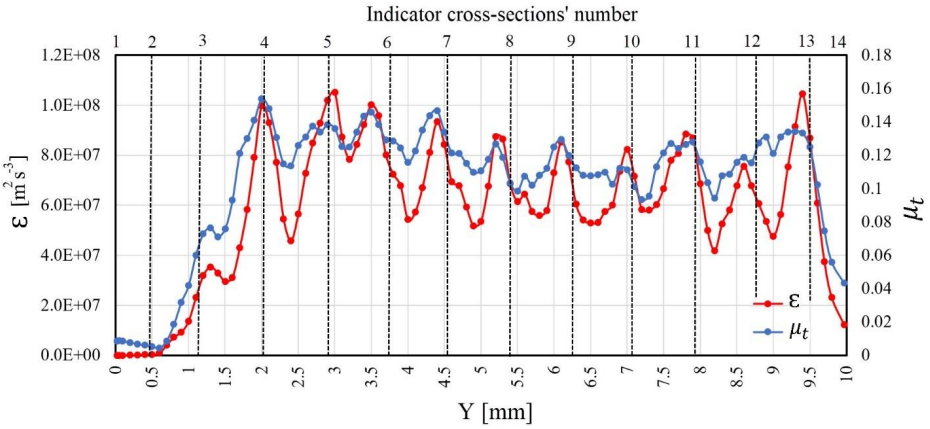

Fig.14: Average ε over different cross-sections (XZ planes) perpendicular to the main flow direction (Y axis).

6. Results for various pressure drops

This section examines the pore-level structure of fluid flow through packed spheres at different Δp. Afterwards, the tortuosity, permeability, turbulence variables, and Reynolds numbers are computed at various Δp values to examine the onset of changes in flow regimes.

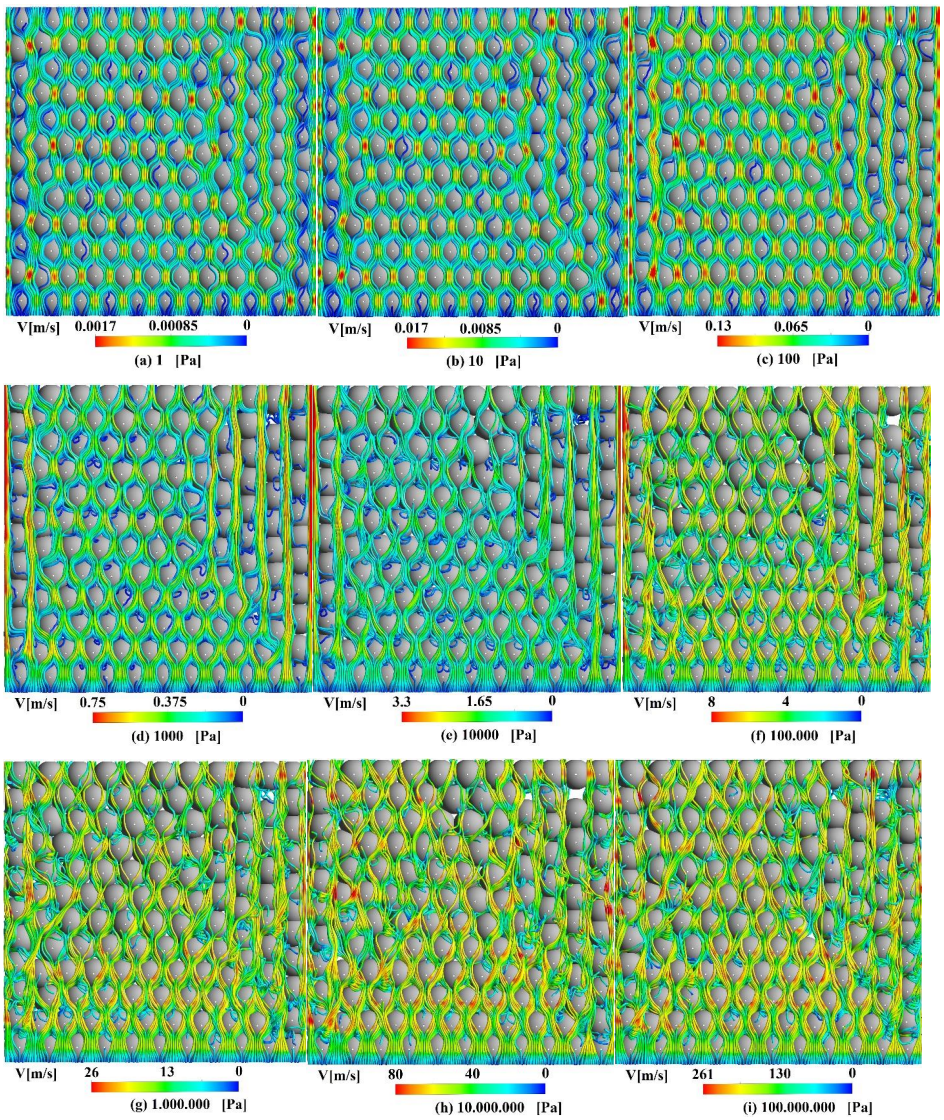

Fig.15: Velocity streamlines at various Δp ranging from 0.1 Pa to 100 MPa.

Figure 15 demonstrates the streamlines at various pressure drops (Δp) to visualize the flow behaviour within the pore space among spheres. As can be seen from the figure, at small values of Δp (< 100 Pa) corresponding to Fig.15a-c, streamlines perfectly follow the internal structure of the porous medium. The streamlines remain parallel to each other and prevent the occurrence of swirling zones. At higher values of Δp, the streamlines become more complex and tortuous. The streamlines are under the influence of boundary layers, wakes, and generally, inertial forces. By increasing Δp, these influences become progressively apparent. This leads to the formation of swirling structures in the flow field.

In this study, we applied the free-slip boundary condition to the side walls of the specimen, as the small specimen investigated is intended to represent a segment of a larger rock formation. However, the highly linear streamlines observed along the right side of the packing in Fig.15 suggest that this boundary condition might simplify the flow dynamics in certain regions.

Research on porous media also relies on tortuosity (τ), which refers to the average deviation of fluid streamlines from straight paths within the material. It has a value greater than or equal to one. A formula is proposed in [65] and [66] to obtain tortuosity (τ) directly from the flow velocity without the measurement of streamlines:

$$\tau \cong \frac{\bar{V}}{\bar{V}_{\bar{y}}} \qquad (12)$$

where $\bar{V}$ is the average value of the flow velocity m/s.

Figure 16 presents the variation of tortuosity (τ) against the pressure drop per unit length $\frac{\text{MPa}}{\text{m}}$. The τ was calculated for both laminar and turbulent flow regimes. By increasing the pressure drop from 1e^{-5} to 3e^{-3} $\frac{\text{MPa}}{\text{m}}$, τ remains constant at 1.1. As stated in [28], a raise in tortuosity by the increase in the velocity can be used as an estimation point for the onset of non-Darcy flow. It occurs at $\Delta P/L$ = 3e^{-3} $\frac{\text{MPa}}{\text{m}}$ which is an accurate approximation of the real value obtained in the following part. In this pressure drop, the value of Re_K is 0.11 which is in agreement with previous research [67]. The laminar model can predict accurately up to $\Delta p = 0.04$ MPa (3.94 MPa/m). As the pressure drop increases up to 100 $\frac{\text{MPa}}{\text{m}}$, the flow pathways become more tortuous, leading to an increase in tortuosity. After that, it remains almost at the same level up to 10000 $\frac{\text{MPa}}{\text{m}}$. The tortuosity of the specimen can be assumed to be approximately 1.35.

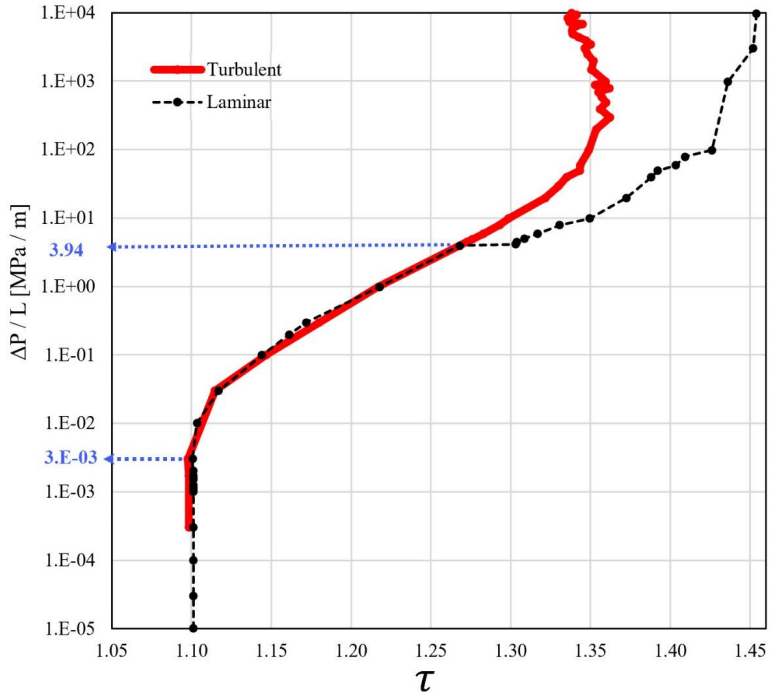

Fig.16. Tortuosity (τ) as a function of pressure drop per unit length [$\frac{\text{MPa}}{\text{m}}$].

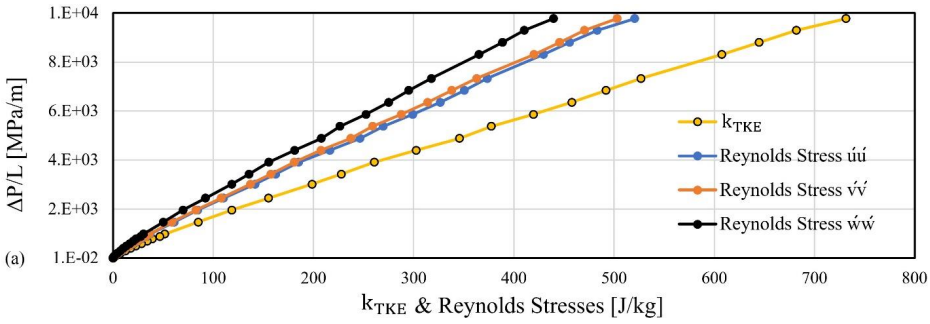

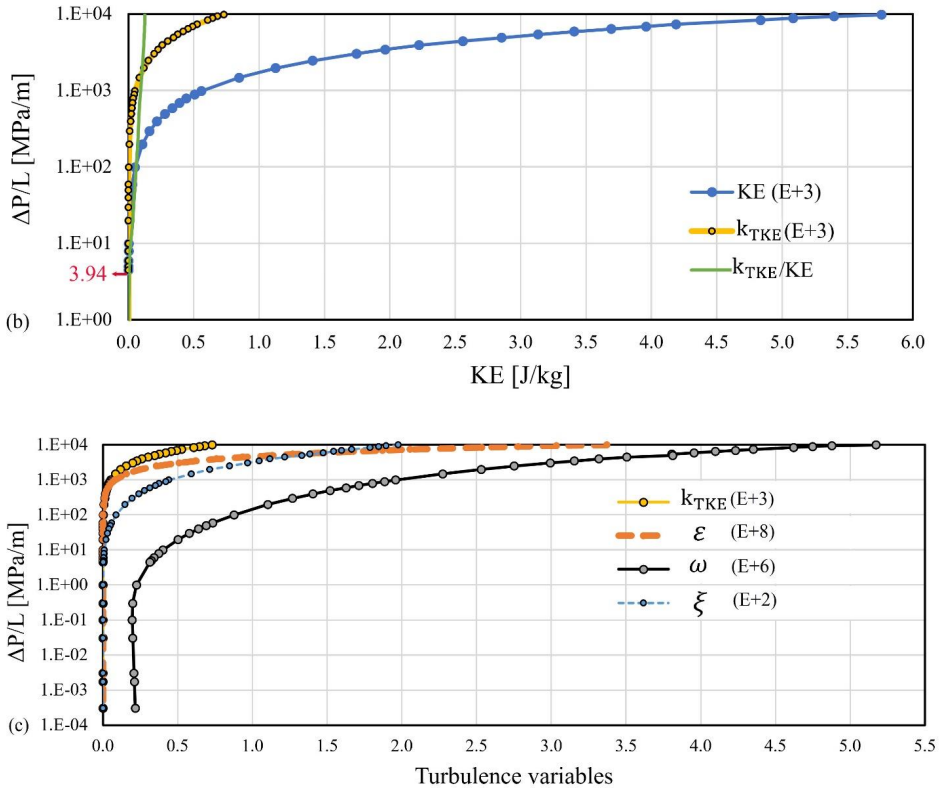

Fig.17: Volume-averaged values of turbulent variables against pressure drop across the 3D domain. The k_{TKE} plot is included in all figures for comparison. (a) Reynolds stress components (b) (total) kinetic energy (KE) over the 3D domain, along with the ratio of k_{TKE} to KE. (c) ω, ε, and viscosity ratio (ξ) across the 3D domain.

Figure 17a-c illustrates the average turbulence variables values across the entire 3D domain relative to the pressure drop. In Fig.17a, k_{TKE} exhibits almost linear growth at high Δp. The variations in the X and Y directions are greater than those in the Z direction, playing a major role in generating k_{TKE}. The amount of k_{TKE} increases from 0 to a maximum of 731 m^2/s^2 at the Δp = 100 MPa which is 12.6% of the macroscopic KE at this point (Fig.17b). The starting point for generating turbulent fluctuations in the flow field (the transition zone from laminar to turbulence) can be

considered as the point with a pressure drop of 3.94 $\frac{\text{MPa}}{\text{m}}$, where the ratio of k_{TKE}/KE is approximately 0.004. This point is highlighted in Fig.17b. The volume averaged values of ε, ξ and eddy frequency are depicted in Fig.17c, along with the $\overline{k_{TKE}}$ for comparison. Figure 17c shows that with increasing Δp, the volume-averaged values of all four quantities grow nonlinearly. Similar to the plot for k_{TKE}, the pressure drop of 3.94 $\frac{\text{MPa}}{\text{m}}$ can be considered as the onset of energy dissipation. The viscosity ratio ξ is equal to 0.25 at this point.

In the simulation, the pressure drop Δp is the main driving factor for transitioning from Darcy to the non-Darcy regime. The Darcy law is valid in the range where a linear relationship exists between Δp and U_s. In this range, the permeability Reynolds Re_K is smaller than 0.1 [67]. However, as noted by Chhabra [68], there is no specific Re number that can be used to distinguish the Darcy from non-Darcy flow regime in a porous medium. Comiti et al. [69] proposed a suitable criterion, considering the termination point of the Darcy regime as the point where the linear term in the pressure drop equation (Eq.2) reduces to less than 99% of the overall pressure drop Δp. This study has investigated and adopted the criterion proposed by Comiti et al. [69] for determining the Darcy and non-Darcy (Forchheimer) regimes.

A non-denominational permeability (K^*) was proposed in [28] to identify the onset of the non-Darcy regime, using a criterion similar to the one proposed in [69]:

$$K^* = \frac{K_{app}}{K_D} \tag{13}$$

where K_D can be obtained directly from Eq.1 or estimated by Eq.7 or 8. K_{app} is the apparent permeability defined as:

$$\frac{1}{K_{app}} = \frac{1}{K_F} + \frac{\rho\beta}{\mu}U \tag{14}$$

Equations 13 and 14 are basically a rearrangement of Eq.2, resulting in the same termination point as that obtained from the criterion proposed by Comiti et al. [69]. Therefore, the point at which K^* reaches 0.99 can be considered as the threshold of the non-Darcy regime using the above criterion. Additionally, the inertial coefficient, β, can be obtained by the slope of the term $\frac{1}{K_{app}}$ against $\frac{\rho}{\mu}U$ curve in the non-Darcy regime [28].

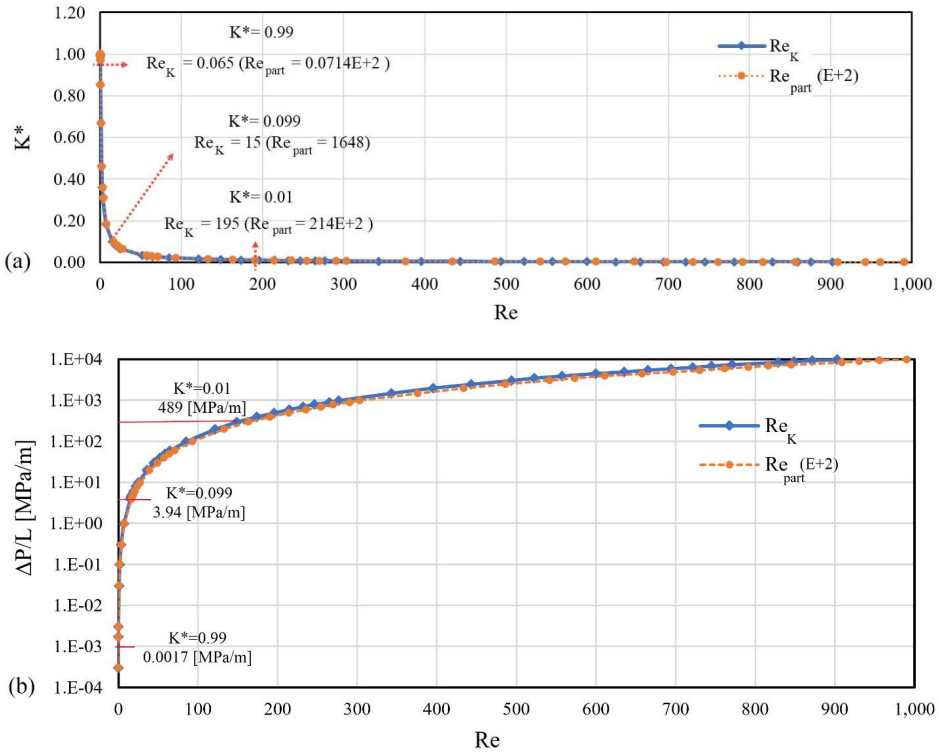

Fig.18. Relationship between Re_K and Re_{part} with (a) dimensionless permeability K^* and (b) pressure drop $\Delta P/L$.

Figure 18a illustrates the dimensionless permeability, K^*, plotted against the permeability/particle Re number. The K^* decreases nonlinearly from 1 (in the viscous-dominated regime) to nearly 0 (in the inertial-dominated regime). The transition from Darcy to the non-Darcy regime occurs at K^*=0.99, corresponding to $Re_K = 0.065$ ($Re_{part} = 7.14$). As stated in [28], Re_K proves to be a more suitable criterion for determining threshold of the non-Darcy regime. Based on our findings from Fig.17b, where the threshold for the 'transient zone' from laminar to turbulent is defined at a pressure drop of $3.94\frac{\text{MPa}}{\text{m}}$, the associated Re number for K^*=0.099, i.e., Re_{part} =1648, can be considered as the threshold for the "transient zone" in Fig.18. At this point, k_{TKE} begins to manifest and gradually intensifies with increasing K^* until it reaches the fully turbulent (inertial-dominated)

regime at K^*=0.01. This regime is attained at Re_K=195 (Re_{part}=21443). At this stage, the first term (viscous term) in the pressure drop equation (Eq.2) constitutes less than 1% of the overall Δp. Figure18b displays the Re number at different pressure drops, with corresponding values of pressure drop for K^*=0.01 and 0.99 given in the figure. At pressure drop points of $0.0017\frac{\text{MPa}}{\text{m}}$, $3.9\frac{\text{MPa}}{\text{m}}$, and $489\frac{\text{MPa}}{\text{m}}$, the flow regime transitions occur. These points indicate shifts to non-Darcy, transient, and fully turbulent regime, respectively.

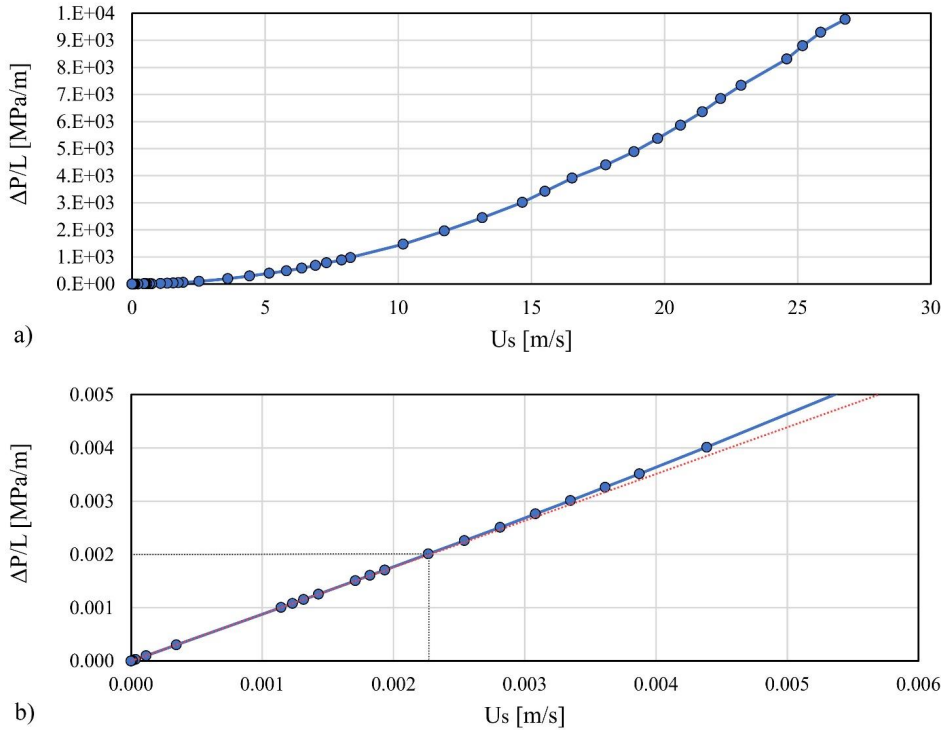

Fig.19: Relationship between pressure drop Δp per unit lentgh [$\frac{\text{MPa}}{\text{m}}$] and superficial velocity [m/s] (a) full Δp range (b) focusing only on low Δp (Darcy zone).

In Fig.19a, it is evident that the superficial velocity undergoes nonlinear changes with the pressure drop. However, when focusing on a narrow range of superficial velocity, as illustrated in Fig.19b, a linear relationship appears. This relationship is associated with the Darcy zone. The point where the slope changes signifies the threshold of the non-Darcy regime. This point is corresponded to a pressure drop of 0.002 $\frac{\mathrm{MPa}}{\mathrm{m}}$ and occurred at U_s= 0.0022 m/s. Finally, Tab.2 presents critical Re numbers coresponding to the transition from Darcy to non-Darcy, from laminar to transient, and to fully turbulent regimes using various criteria. As shown in table, the U_s diagram (Fig.19) identifies the value of $K^* \cong 0.99$ as the onset of the non-Darcy regime. The assumption of K^*=0.99 as the threshold of the non-Darcy regime (as suggested in [69]) is found to be an accurate criterion, while K^*=0.97 which was obtained based on τ diagram (Fig.16), can be considered as an acceptable engineering estimation. In some earlier studies, the Reynolds number (Re) for the fluid flow in packed particles is defined as $\emptyset \times \mathrm{Re}_{\mathrm{part}}$. The onset of the non-Darcy regime based on this Re definition is reported to be within the range of 1-15 (according to [70]), 0.1-75 (according to [71]) and 3-10 (according to [72]). The assumption of K^*=0.97 leads to $\emptyset \times \mathrm{Re}_{\mathrm{part}}$ = 4.07 for the transition from Darcy to the non-darcy regime. This value aligns well with findings from literature. Ergun used a diffrent defination of the Re number for the flow past packed particles as $\frac{\emptyset}{(1-\emptyset)} \times \mathrm{Re}_{\mathrm{part}}$. Based on this defination, threshold occurrences fall between 3 and 10 [41]. The results from our study also agree with [41], as the threshold of the non-Darcy regime based on Ergun's definition of Re was obtained as 6.11. This value falls within the range reported by Ergun.

Tab.2: Critical Re, pressure drop (ΔP per unit length), and ξ for the transition between flow regimes (onset of change from Darcy to non-Darcy, initiation of the transient zone from laminar to turbulent, and the onset of the fully inertial regime , i.e., fully turbulent).

	Onset estimated by:				
	τ	U_s	K^*		
	Non -Darcy regime	Non -Darcy regime	Non -Darcy regime	Transition from laminar to turbulent (generating turbulences)	Fully turbulent regime
K^*	0.97	0.986	0.99	0.099	0.01
ΔP [MPa]	$30e^{-6}$	$20e^{-6}$	$17e^{-6}$	0.039	4.87
$\Delta P/L$ [MPa/m]	0.003	0.002	0.0017	3.9	489
Re_K	0.11	0.076	0.065	15	195.44
Re_{part}	12.3	8.37	7.14	1648	21443
ξ	$6e^{-7}$	$1.9e^{-7}$	$1.2e^{-7}$	0.25	27.75

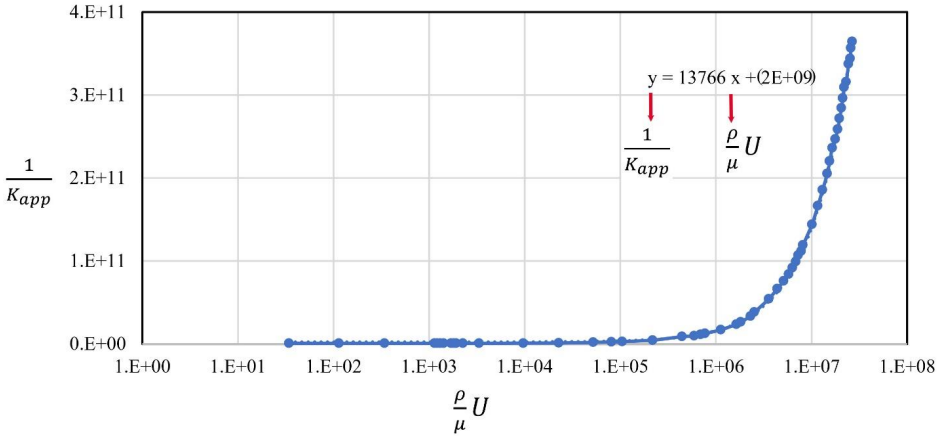

Fig.20. The diagram depicting $\frac{1}{K_{app}}$ [m^{-2}] against $\frac{\rho}{\mu}U$ [m^{-1}] to calculate β.

Based on Eq.15, the inertial term coefficient, β, can be calculated by finding the slope of the curve $\frac{1}{K_{app}}$ against ro $\frac{\rho}{\mu}U$ curve. As can be seen in Fig.20 , the obtained β coefficient is 13747, whereas, based on Ergun's equation (Eq.2), it is estimated to be 24629. Table 3 compares our calculated values of K_D and β with well-known equations. Various empirical equations for obtaining K_D and β factors (detailed in [73]), can yield a wide range of estimations for K_D and β (as exemplified in [28]). Additionally, the non-spherical shape of our particles, arising from overlaps between spheres, introduces some discrepancies between the results of our study and those derived from these equations.

Tab.3. Predicted permeability and inertial coefficient.

	Kozeny–Carman (Eq.14)	Ergun (Eq.2)	van der Hoef (Eq.8)	our calculation	
				(Darcy (Eq.1))	(K^* (Eq.14))
K_D	0.734E-9	0.88E-9	0.73 e-9	1.147E-9	---------
β	------	24629.57	--------	--------	13747

7. Summary, conclusion and future directions

In the presented work, flow inside a porous medium across a wide range of Reynolds numbers was studied and visualized. Key innovations include the development of a new validation and calibration method for the 2D DEM-CFD models, which addresses the challenge of limited experimental data on fluid flow characteristics in densely packed granules, particularly under high pressure conditions. Another objective was to analyze the flow characteristics at various pressure drops (ranging from 0 to 100 MPa) within the porous domain and to distinguish the significant flow regimes. The turbulent variables and flow characteristics were visualized with a particular focus on a pressure drop of 30 MPa. We compared the results between turbulent and laminar flow conditions. The main findings for the unique packing of spheres are:

- **Novel Validation Method**: A novel method for validating and calibrating simplified 2D DEM-CFD models is developed. The optimal specimens were designed, consisting of a single layer of spheres, and analyzed in detail. The validity of the 3D-FVM model was confirmed through meticulous validation against experimental and numerical data from the literature.

- **Detailed Flow Analysis**: The flow characteristics within porous specimen were comprehensively studied under varying conditions, spanning from Darcy to fully turbulent regimes ($0 < Re_{part} <$ 100.000). The BSL approach showed accurate simulation performance in both laminar and turbulent regimes.

- **Flow Regimes Analysis:**
    a. The onset of the non-Darcy regime within this special sphere packing was estimated as $\mathrm{Re_K} = 0.11$ ($\mathrm{Re_{part}} = 12.3$) by three different methods.
    b. Laminar flow continued up to $\mathrm{Re_{part}}$= 1648, transitioning to full turbulence beyond $\mathrm{Re_{part}}$= 21443.
    c. Novel criteria were proposed for the transient and fully turbulent regimes: $K^* < 0.099$ and $K^* < 0.01$, respectively.

- **Computing tortuosity:** The tortuosity in this geometry was obtained as 1.35.

This study employs a single monolayer of spheres for simulations, which, while providing valuable insights, may not fully capture the complexity of realistic porous matrices. The geometric constraint of having all sphere centers lie within a single plane results in a structured packing, which does not accurately represent the natural disordered packing of real porous materials. This limitation could influence the generalizability of the quantitative conclusions, particularly those in Tables 2 and 3. Also, simulations were only performed for the porosity of 34% with a specific material property, and hence, in future works, extensive studies using advanced methodologies should be carried out to examine various porosities and material properties. Useful methodologies include the Response Surface Method (RSM) (e.g. [74]) and machine learning techniques (e.g., [75], [76]). In addition, due to difficulty in artificial specimen preparation for experimental studies or inhomogeneous structure of natural specimens like rocks, it is suggested to use additive manufacturing processes for the fabrication of porous specimens with complex and customized geometries [77]-[79]. By using additive manufacturing, researchers may effectively manipulate porosity and customize material characteristics.

Acknowledgments

The present study was supported by the research project "*Fracture propagation in rocks during hydro-fracking – experiments and discrete element method coupled with fluid flow and heat transport*" (years 2019-2022), financed by the National Science Centre (NCN) (UMO-2018/29/B/ST8/00255).

Contributions:

Rezvan Abdi: data curation, software, visualization, validation, investigation, methodology, writing-original draft preparation

Marek Krzaczek: writing-reviewing and editing, methodology, supervision

Meisam Abdi: writing-reviewing and editing, supervision

References:

[1] R. Abdi, M. Krzaczek, J. Tejchman. Comparative study of high-pressure fluid flow in densely packed granules using a 3D CFD model in a continuous medium and a simplified 2D DEM-CFD approach, *Granular Matter*, 2022. 24(1):1-25.

[2] R. Abdi, M. Krzaczek, J. Tejchman. Simulations of high-pressure fluid flow in a pre-cracked rock specimen composed of densely packed bonded spheres using a 3D CFD model and simplified 2D coupled CFD-DEM approach, *Powder Technology*, 2023. 118238.

[3] V. Patil, J. Liburdy. Flow Regime Characteristics in Porous Media Flows at High Reynolds Numbers. *Fluids Engineering Division Summer Meeting*, *American Society of Mechanical Engineers.* 2012. 44755:731-737.

[4] N.K. Nath, K. Mitra. Mathematical modeling and optimization of two-layer sintering process for sinter quality and fuel efficiency using genetic algorithm. *Materials and Manufacturing Processes*. 2005. 20(3):335–349.

[5] A. Ljung, V. Frishfelds, T.S. Lundström, B.D. Marjavaara: Discrete and continuous modeling of heat and mass transport in drying of a bed of iron ore pellets. *Drying Technology*. 2012. 30(7):760–773.

[6] C. Williams, J. Summerscales, S. Grove. Resin infusion under flexible tooling (RIFT): a review. *Applied Science and Manufacturing*. 1996. 27(7):517–524.

[7] H. Andersson, T. Lundström, N. Langhans. Computational fluid dynamics applied to the vacuum infusion process. *Polymer composites*. 2005. 26(2):231–239.

[8] W. Johnston, A. Dybbs, R. Edwards, Measurement of fluid velocity inside porous-media with a laser anemometer. *Physics of Fluids*. 1975. 18(7):913- 914.

[9] I. Kececioglu, Y. Jiang. Flow through porous media of packed spheres saturated with water. 1994. 164-170.

[10] P. Kundu, V. Kumar, I.M. Mishra. Experimental and numerical investigation of fluid flow hydrodynamics in porous media: Characterization of pre-Darcy, Darcy and non-Darcy flow regimes, *Powder Technology,* 2016, 303: 278-291.

[11] S. Khayamyan, T.S. Lundström, P. Gren, H. Lycksam, and J.G.I. Hellström. Transitional and turbulent flow in a bed of spheres as measured with stereoscopic particle image velocimetry.*Transport in Porous Media.* 2017.117:45-67.

[12] L.W. Rong, K.J. Dong, A.B. Yu. Lattice-Boltzmann simulation of fluid flow through packed beds of spheres: effect of particle size distribution, *Chemical Engineering Science*, 2014, 116: 508-523.

[13] A. Tariq, Z. Liu. Heat transfer and friction factor correlations for slip gaseous fluid flow in confined porous medium with pore-scale LBM modelling. *International Journal of Thermal Sciences.* 2022. 173:107382.

[14] L.W. Rong, K.J. Dong, A.B. Yu. Lattice-Boltzmann simulation of fluid flow through packed beds of uniform spheres: Effect of porosity. *Chemical Engineering Science.* 2013. 99:44-58.

[15] A. Nabovati, A.C.M. Sousa. Fluid flow simulation in random porous media at pore level using lattice Boltzmann method. *New trends in fluid mechanics research.*2007. 518-521.

[16] M.A. van der Hoef, R. Beetstra, J.A.M. Kuipers. Lattice-Boltzmann simulations of low-Reynolds-number flow past mono-and bidisperse arrays of spheres: results for the permeability and drag force, *Journal of Fluid Mechanics,* 2005, 528: 233-254. Hamun 12

[17] P. Yang, Z. Wen, R. Dou, X. Liu. Permeability in multi-sized structures of random packed porous media using three-dimensional lattice Boltzmann method, *International Journal of Heat and Mass Transfer,* 2017, 106: 1368-1375.

[18] A. Kakouei, A. Vatani, M. Rasaei, B.S. Sola, H. Moqtaderi. Cessation of Darcy regime in gas flow through porous media using LBM: Comparison of pressure gradient approaches. *Journal of Natural Gas Science and Engineering*. 2017. *45*:693-705.

[19] M.J. Baker, G.R. Tabor. Computational analysis of transitional air flow through packed columns of spheres using the finite volume technique, *Computers & Chemical Engineering,* 2010, 34(6): 878-885.

[20] P.R. Gunjal, V.V. Ranade, R.V. Chaudhari. Computational study of a single-phase flow in packed beds of spheres, *AIChE Journal*, 2005. 51(2): 365-378.

[21] Y. Kutsovsky, L. Scriven, H. Davis, B. Hammer. NMR imaging of velocity profiles and velocity distributions in bead packs. *Physics of Fluids*. 1996. 8(4):863–871.

[22] L.F. Gladden, B.S. Akpa, L.D. Anadon, J.J. Heras, D.J. Holland, M.D. Mantle, S. Matthews, C. Mueller, M.C. Sains, A.J. Sederman. Dynamic MR imaging of single-and two-phase flows. *Chemical Engineering Research and Design.* 2006. 84:272-281.

[23] C. Chang, A.T. Watson. NMR imaging of flow velocity in porous media. *AIChE Journal*. 1999. 45(3):437–444.

[24] S. Khayamyan, T.S. Lundström. Interaction between the flow in two nearby pores within a porous material during transitional and turbulent flow. *Journal of Applied Fluid Mechanics*. 2015. 8(2):281–290.

[25] S. Khayamyan, T.S. Lundström, L.H. Gustavsson. Experimental investigation of transitional flow in porous media with usage of a pore doublet model. *Transport in porous media.* 2014. 101(2): 333–348.

[26] T. Suekane, Y. Yokouchi. Hirai S. Inertial flow structures in a simple-packed bed of spheres. *AIChE Journal*, 2003. 49(1):10-17.

[27] R. Caulk, L. Scholtès, M. Krzaczek, B. Chareyre. A pore-scale thermo–hydro-mechanical model for particulate systems. *Computer Methods in Applied Mechanics and Engineering. 2020.* 372:113292.

[28] B.P. Muljadi, M.J. Blunt, A.Q. Raeini, B. Bijeljic. The impact of porous media heterogeneity on non-Darcy flow behaviour from pore-scale simulation, *Advances in Water Resources*, 2016, 95, 329-340.

[29] Ma, Xinfang. A new simulation approach to model complex fracture networks in the shale formation considering gas desorption. 2016.

[30] P. Venkataraman, P.R.M. Rao, Darcian, transitional and turbulent flow through porous media, *Journal of hydraulic engineering*. 1998. 124:840–84.

[31] Ö. Bagci, N. Dukhan, M. Özdemir. Flow regimes in packed beds of spheres from predarcy to turbulent, Transport in porous media. 2014. 104:501–520.

[32] J. Kozeny. Uber kapillare leitung der wasser in boden. *Royal Academy of Science, Vienna*.

1927.136:271-306.

[33] P.C. Carman. Fluid flow through granular beds. *Trans. Inst. Chem. Eng.* 1937. *15*:150-166.

[34] P.C. Carman. Flow of gases through porous media. *Buttervvorth Scientific Pub*. 1956.

[35] R.M. Fand, B.Y.K. Kim, A.C.C. Lam, R.T. Phan. Resistance to the flow of fluids through simple and complex porous media whose matrices are composed of randomly packed spheres, *J. Fluids Eng*. Sep 1987, 109(3): 268-273.

[36] S. Liu, J.H. Masliyah. Single fluid flow in porous media. *Chemical Engineering Communications*. 1996. 653:148–150

[37] R. Meyer, F.F. Krause. Experimental evidence for permeability minima at low velocity gas flow through naturally formed porous media. *Journal of Porous Media.* 1998. *1*(1).

[38] M. Fourar, G. Radilla, R. Lenormand, C. Moyne. On the non-linear behavior of a laminar single-phase flow through two and three-dimensional porous media. *Advances in Water resources*. 2004. 27(6):669–77.

[39] MS. Newman, X. Yin. Lattice Boltzmann simulation of non-Darcy flow in stochastically generated 2D porous media geometries. SPE *Journal.* 2013.18:12–26.

[40] S.P. Burke, W.B. Plummer. Gas flow through packed column. *Industrial & Engineering Chemistry.* 1928. 1196–1200.

[41] S. Ergun. Fluid flow through packed columns. *Chem. Eng. Prog*. 1952. 48:89–94.

[42] M. Leva, Fluidisation. *New York: McGraw-Hill Book Company*. 1959.

[43] T.F. MacDonald, M.S. El-Sayer, K. Mow, F.A.L. Dullen. Flow through porousmedia: The Ergun equation revisited. *Industrial and Engineering Chemistry Fundamentals*. 1979. 18:199–208.

[44] P.J.D. Plessis, S. Woudberg. Pore-scale derivation of the Ergun equation to enhance its adaptability and geralization. Chemical Engineering Science. 2008. 63:2576–2586.

[45] L. Lebon, L. Oger, J. Leblond, J.P. Hulin, N.S. Martys, L.M. Schwartz. Pulsed gradient NMR measurements and numerical simulation of flow velocity distribution in sphere packings. *Physics of Fluids*, 1996. 8:293-301.

[46] M. Krzaczek, M. Nitka, J. Kozicki, J. Tejchman. Simulations of hydro-fracking in rock mass at meso-scale using fully coupled DEM/CFD approach, *Acta Geotechnica*, 2020. 15(2): 297-324.

[47] M. Krzaczek, M. Nitka, J. Tejchman. Effect of gas content in macropores on hydraulic fracturing in rocks using a fully coupled DEM/CFD approach, *International Journal for Numerical and Analytical Methods in Geomechanics*, 2021. 45(2):234-264.

[48] M. Krzaczek, M. Nitka, J. Tejchman. A novel DEM based pore-scale thermo-hydro-mechanical model, *Computational Modelling of Concrete and Concrete Structures.* 2022, CRC Press, 596-604.

[49] M. Krzaczek, M. Nitka, J. Tejchman. Modeling of capillary fluid flow in concrete using a DEM-CFD approach, *Computational Modelling of Concrete and Concrete Structures*. 2022, CRC Press, 572-581.

[50] K. Boomsma, D. Poulikakos. The effects of compression and pore size variations on the liquid flow characteristics in metal foams, *J. Fluids Eng*., 2002. 124(1):263-272.

[51] CFX, Ansys CFX Documentation. ANSYS Inc., USA, 2019.

[52] R.P. Chhabra, J. Comiti, I. Machač. Flow of non-Newtonian fluids in fixed and fluidised beds. *Chemical Engineering Science.* 2001. 56(1):1-27.

[53] D. Seguin, A. Montillet, J. Comiti. Experimental characterisation of flow regimes in various porous media, I: Limit of laminar flow regime. *Chemical Engineering Science.* 1998. 53(21), 3751-3761.

[54] D. Seguin, A. Montillet, J. Comiti, F. Huet. Experimental characterization of flow regimes in various porous media, II: Transition to turbulent regime. *Chemical engineering science.* 1998. 53(22), 3897-3909.

[55] A. Grabowski, M. Nitka. 3D DEM simulations of basic geotechnical tests with early detection of shear localization. *Studia Geotechnica et Mechanica*. 2021. 43(1), 48-64.

[56] M. Nitka, A. Grabowski. Shear band evolution phenomena in direct shear test modelled with DEM. *Powder Technology*. 2021. 391, 369-384.

[57] A. Grabowski, M. Nitka, J. Tejchman. 3D DEM simulations of monotonic interface behaviour between cohesionless sand and rigid wall of different roughness. *Acta Geotechnica*. 2021. 16(4),

1001-1026.

[58] ANSYS User's Manual Revision 5.2, *ANSYS*, 1995. 1.

[59] S.A. Logtenberg, A.G. Dixon. Computational fluid dynamics studies of fixed bed heat transfer. *Chemical Engineering and Processing: Process Intensification*.1998. 37:7-21.

[60] N. Rezazadeh, R. Abdi, Numerical simulation of natural convection from a pair of hot cylinders in a cold square enclosure in different boundary conditions, *Frontiers in heat and mass transfer*, 2016. 7.

[61] R. Abdi, N. Rezazadeh, M. Abdi. Investigation of passive oscillations of flexible splitter plates attached to a circular cylinder*, Journal of Fluids and Structures*, 2019. 84: 302-317.

[62] R. Abdi, N. Rezazadeh, M. Abdi. Reduction of fluid forces and vortex shedding frequency of a circular cylinder using rigid splitter plates, *European Journal of Computational Mechanics,* 2017. 26(3): 225-244.

[63] F. Eydi, A. Mojra, R. Abdi. Comparative analysis of the flow control over a circular cylinder with detached flexible and rigid splitter plates, *Physics of Fluids*, 2022. 34:113604.

[64] MHJ. Pedras, JS. Marcelo, de. Lemos. Simulation of turbulent flow in porous media using a spatially periodic array and a low Re two-equation closure. *Numerical Heat Transfer: Part A: Applications*. 2001. 39:35-59.

[65] A. Koponen, M. Kataja, J. Timonen. Tortuous flow in porous media. *Physical Review E*. 1996. 54:406–10.

[66] A. Duda, Z. Koza, M. Matyka. Hydraulic tortuosity in arbitrary porous media flow. *Physical Review E*. 2011. 84:036319.

[67] J. Lage. *The fundamental theory of flow through permeable niedia from darcy to turbulence.* Transport phenomena in porous media, 1998, 1.

[68] R. Chhabra. Bubbles, drops, and particles in non-Newtonian fluids. *Chemical Industries/Taylor & Francis*. 2006. ISBN 9781420015386.

[69] J. Comiti, N. Sabiri, A. Montillet. Experimental characterization of flow regimes in various porous media III: limit of Darcy's or creeping flow regime for Newtonian and purely viscous non-Newtonian fluids. *Chemical engineering science.* 2000. 55(15):3057–6.

[70] S. Hassanizadeh, W. Gray. High velocity flow in porous media. *Transport in Porous Media*. 1987. 2(6):521–31.

[71] A. Scheidegger. The physics of flow through porous media. *University of Toronto Press*; 1974. ISBN 9780802018496.

[72] J. Bear. Dynamics of fluids in porous media. *Dover Publications*. 1972. ISBN 978- 0-486-65675-5.

[73] D. Li, T.W. Engler. Literature review on correlations of the non-Darcy coefficient. In *SPE permian basin oil and gas recovery conference*. 2001.

[74] B. Adibimanesh, M.B. Ayani, H. Khozeymeh-Nezhad, S. Polesek-Karczewska. Applying response surface method to optimize the performance of a divergent-chimney solar power plant. *Sustainable Energy Technologies and Assessments*. 2021. 48:101593.

[75] A. Dehestani, F. Kazemi, R. Abdi, M. Nitka. Prediction of fracture toughness in fibre-reinforced concrete, mortar, and rocks using various machine learning techniques. *Engineering Fracture Mechanics*. 2022. 276, 108914.

[76] B. Adibimanesh, S. Polesek-Karczewska, F. Bagherzadeh, P. Szczuko, T. Shafighfard, Energy consumption optimization in wastewater treatment plants: Machine learning for monitoring incineration of sewage sludge. *Sustainable Energy Technologies and Assessments*. 2023. 56, 103040.

[77] A. Panesar, M. Abdi, D. Hickman, I. Ashcroft. Strategies for functionally graded lattice structures derived using topology optimisation for additive manufacturing, *Additive Manufacturing*. 2018. 19:81-94.

[78] H.M.A. Ali, M. Abdi, Y. Sun. Insight into the mechanical properties of 3D printed strut-based lattice structures. *Progress in Additive Manufacturing.* 2023, *919–931.*

[79] S. Afkhami, M. Abdi, R. Baserinia. Influence of Surface Area on Dissolution of Additively Manufactured Polyvinyl Alcohol Tablets. *International Journal of Mechanical and Industrial Engineering*, 2024, 18(3), 72-75.